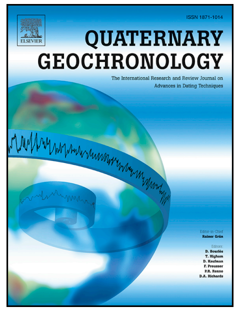

A multi-dating approach to age-modelling long continental records: The 135 ka El Cañizar de Villarquemado sequence (NE Spain)

B.L. Valero-Garcés, P. González-Sampériz, G. Gil Romera, B.M. Benito, A. Moreno, B. Oliva-Urcia, J. Aranbarri, E. García-Prieto, M. Frugone, M. Morellón, L.J. Arnold, M. Demuro, M. Hardiman, S.P.E. Blockley, C.S. Lane

PII: S1871-1014(18)30115-8

DOI: https://doi.org/10.1016/j.quageo.2019.101006

Article Number: 101006

Reference: QUAGEO 101006

To appear in: *Quaternary Geochronology*

Received Date: 9 October 2018

Revised Date: 22 March 2019

Accepted Date: 14 June 2019

Please cite this article as: Valero-Garcés, B.L., González-Sampériz, P., Gil Romera, G., Benito, B.M., Moreno, A., Oliva-Urcia, B., Aranbarri, J., García-Prieto, E., Frugone, M., Morellón, M., Arnold, L.J., Demuro, M., Hardiman, M., Blockley, S.P.E., Lane, C.S., A multi-dating approach to age-modelling long continental records: The 135 ka El Cañizar de Villarquemado sequence (NE Spain), *Quaternary Geochronology* (2019), doi: https://doi.org/10.1016/j.quageo.2019.101006.

A multi-dating approach to age-modelling long continental records: the 135 ka El Cañizar de Villarquemado sequence (NE Spain)

B.L. Valero-Garcés[1,2]; P. González-Sampériz[1]; G. Gil Romera[1,3]; B. M. Benito[4]; A. Moreno[1,2]; B. Oliva-Urcia[5]; J. Aranbarri[6]; E. García-Prieto[1]; M. Frugone[7,2]; M. Morellón[8]; L.J. Arnold[9]; M. Demuro[9]; M. Hardiman[10]; S.P.E. Blockley[11]; C.S. Lane[12]

1. Pyrenean Institute of Ecology (IPE) – CSIC. Avda Montañana 1005. E-50059 Zaragoza, Spain.
2. Laboratorio Internacional de Cambio Global, CSIC, PUC, UFRJ, Avda Montañana 1005. E-50059 Zaragoza, Spain.
3. Department of Geography and Environmental Sciences, Llandinam building, Penglais Campus. Aberystwyth University SY233DB, Aberystwyth, United Kingdom.
4. Ecological and Environmental Change Research Group, Department of Biological Sciences, University of Bergen, Norway.
5. Department of Geology and Geochemistry, Faculty of Sciences, Universidad Autónoma de Madrid. C/ Francisco Tomás y Valiente 7. Campus de Cantoblanco, E-28049 Madrid, Spain.
6. Department of Geography, Prehistory and Archaeology, University of the Basque Country, Francisco Tomás y Valiente, s/n. E-01006 Vitoria-Gasteiz, Spain.
7. Department of Ecology. Pontificia Universidad Católica de Chile, Avda. Alameda, Santiago, Chile.
8. CITIMAC, University of Cantabria. Avenida de los Castros s/n. E-39005 Santander (Cantabria), Spain.
9. School of Physical Sciences, Environment Institute, and Institute for Photonics and Advanced Sensing (IPAS), University of Adelaide, North Terrace Campus, Adelaide, SA, 5005, Australia.
10. Department of Geography, University of Portsmouth, Portsmouth, PO1 3HE, UK.
11. Centre for Quaternary Research, Department of Geography, Royal Holloway, University of London, Egham, Surrey, TW2 0SE, UK.
12. Department of Geography, University of Cambridge, Downing Place, Cambridge, CB2 3EN, UK.

ABSTRACT.

We present the multidisciplinary dating approach - including radiocarbon, Uranium/Thorium series (U/Th), paleomagnetism, single-grain Optical Stimulated Luminescense (OSL), Infrared Stimulated Luminescence (IRSL) and tephrochronology -

used for the development of an age model for the Cañizar de Villarquemado sequence (VIL) for the last ca. 135 ka. We describe the protocols used for each technique and discuss the positive and negative results, as well as their implications for interpreting the VIL sequence and for dating similar terrestrial records. In spite of the negative results of some techniques, particularly due to the absence of adequate sample material or inaccurate analytical precision, the multi-technique strategy employed here is essential to maximize the chances of obtaining robust age models in terrestrial sequences. The final Bayesian age model for VIL sequence includes 16 AMS ^{14}C ages, 9 OSL ages and 5 previously published IRSL ages, and the accuracy and resolution of the model are improved by incorporating information related to changes in accumulation rate, as revealed by detailed sedimentological analyses. The main paleohydrological and vegetation changes in the sequence are coherent with global Marine Isotope Stage (MIS) 6 to 1 transitions since the penultimate Termination, although some regional idiosyncrasies are evident, such as higher moisture variability than expected, an abrupt inception of the last glacial cycle and a resilient response of vegetation in Mediterranean continental Iberia in both Terminations.

KEYWORDS: Bayesian Age model, Radiocarbon, OSL, IRSL, Last Glacial Cycle, Mediterranean, Continental sequences

1. INTRODUCTION

Major advances in paleoclimate research have been made possible only after improving numerical dating methods, reducing the time uncertainties of reconstructed changes and consequently facilitating our ability to precisely correlate ice, marine and terrestrial records along spatial and temporal transects. Only with independent and robust age models we can test 'leads' and 'lags' in teleconnections between the atmospheric, marine, terrestrial and cryospheric realms (Hoek et al., 2008) and understand spatial patterns and mechanisms behind abrupt climate fluctuations, such as those documented within the last glacial cycles (Broecker, 2000).

During the last decades, the scientific community has made a significant effort to recover new, long continental sequences, extending beyond the last glacial cycle from classical sites such as Grande Pile (Woillard, 1978), Les Echets (de Beaulieu and Reille, 1989), Velay (Reille et al., 2000), Monticchio (Allen and Huntley, 2009), Ioannina (Tzedakis et al., 2003), or Tenaghi Philippon (Tzedakis et al., 2006). Several outstanding long sequences have been obtained thanks to international initiatives such as the International Continental Scientific Drilling Program (ICDP, https://www.icdp-online.org/home/) (e.g., Lake Titicaca (Fritz et al., 2007), Potrok Aike (Zolitschka et al., 2013), Dead Sea (Stein et al., 2011), Lake Van (Litt et al., 2009), Petén Itzá (Hodell et al., 2008), El'gygytgyn (Melles et al., 2012), Lake Ohrid (Lézine et al., 2010; Zanchetta et al., 2016), Lake Chalco (Brown et al., 2012), Lake Junin (Rodbell and Abbott, 2012*),* and Towuti in Indonesia (Rusell et al. 2016). These long sequences span several glacial cycles and contain a detailed history of vegetation, environmental and climate changes. However, in all cases, obtaining a robust chronology has remained a challenge. The exceptions to this rule are the long, continuous, annually laminated terrestrial records able to produce absolute and independent varve chronologies, such as Lake Suigetsu in central Japan for the last 70,000 years (Ojala et al. 2012) or well-dated speleothems that accurately cover long time periods, sometimes with excellent resolution (Wang et al., 2001; Pérez-Mejías et al., 2017). Unfortunately, these records are uncommon.

Due to the difficulties of obtaining independent, numerical, reliable and robust chronologies, most of the well-known long traditional sequences rely on either directly or indirectly tuning to orbital configurations or ice core chronologies (Tzedakis et al., 2006). This tuning approach precludes the correct identification of either regional and local particularities or potential leads and lags on different spatial and chronological scales (Brauer et al., 2007).

A combination of different dating techniques depending on the age and type of material is commonly applied to resolve the timing of past events in long terrestrial sequences. Radiocarbon dating is the most commonly used for the last 50,000 years. Though longer calibration curves have become available during the last decade (Reimer et al., 2004, 2009, 2013), this technique is currently limited to the last 30-40 ka and errors of more than several hundred years are frequent, particularly beyond the Last Glacial Maximum (LGM). Another limitation of radiocarbon dating in terrestrial sequences is the frequent low presence of terrestrial organic remains suitable for dating, particularly in semi-arid areas, as well as the occurrence of reworking processes (González-Sampériz et al., 2008; Valero-Garcés and Moreno, 2011; Lionello et al., 2012). U/Th series dating, commonly applied to speleothems, has been also used in lacustrine sequences (Placzek et al., 2006a) but its applicability depends on the presence of highly pure endogenic carbonate in the lacustrine sediments (Bischoff and

Cummins, 2001; Placzek et al., 2006a,b). Paleomagnetic dating based on geomagnetic excursions, inclination and/or declination changes requires a minimum amount of ferromagnetic minerals carrying a primary (acquired at the time of the sedimentation) magnetic signal that clearly define the paleomagnetic characteristic components along the sequence (Johnson et al., 1948). For measurements of declination, methods are needed to precisely record the original orientation of sampled sediment. Tephras provide punctual, numerical, highly accurate ages (e.g., Zanchetta et al., 2011), but discrete ash-layers are not always preserved in terrestrial settings and even cryptotephras are sometimes difficult to detect in lacustrine sediments (Davies, 2015). Despite improvements in the identification and analysis of microscopic volcanic ash layers and cryptotephras transported through very long distances (Blockley et al., 2005; Lane et al., 2017), the use of this technique is spatially limited to regions where material derived from known and previously dated eruptions was deposited and preserved. Luminescence dating techniques such as optically stimulated luminescence (OSL) and infrared stimulated luminescence (IRSL) only require a relatively small amount of siliciclastic material to determine the burial age of terrestrial sediment sequences (the last time since sunlight exposure). However, in spite of recent developments, (e.g., single grain techniques or extended-range approaches; Murray and Roberts, 1997; Arnold et al., 2015), the suitability of luminescence dating techniques may be compromised by certain depositional or post-depositional complications and the analytical precision of these techniques is sometimes sub-optimal for high-resolution studies.

In summary, most of the available dating methods in terrestrial sequences require certain amounts of specific sediment components and it is unlikely that a single technique can provide a universally robust, high resolution chronology. Additionally, a unique problem of long terrestrial records such as lacustrine sequences compared to marine or speleothem records is the larger temporal and spatial variability of sedimentary facies and depositional environments (Cohen, 2003). Within the same sedimentary basin and in the same site, even when located at the deepest part of the basin, depositional dynamics could have greatly changed during the last glacial cycles and sedimentation rates sometimes vary by several orders of magnitude. Thus, linear extrapolation of sedimentation rates without considering these changes in sedimentary facies produces age models with large errors.

In this paper we summarize the efforts to construct an independent robust age model for a long lacustrine sequence from Southwestern Europe: El Cañizar de Villarquemado paleolake (hereafter referred as VIL). The Iberian Peninsula constitutes a sensitive area to reconstruct past hydrological changes (Giorgi and Lionello, 2008; García-Ruiz et al., 2011; Valero-Garcés and Moreno, 2011 and references therein; Morellón et al., 2018) and due to its particular location, with the influence of mid latitude and sub-tropical forcings and a strong Mediterranean - Atlantic climatic gradient, it is a unique place to study the interplays of atmospheric patterns during the last glacial cycles (Lionello et al., 2012; Tzedakis, 2007) and their environmental impacts on the continents through the Late Quaternary (e.g., Carrión and Leroy 2010 and references therein; Magri et al., 2017). Previous research has demonstrated the potential of this site as a recorder of hydrological and vegetation changes in semi-arid continental regions of the Iberian Peninsula during the last ca. 120-130 ka (Moreno et al., 2012; González-Sampériz et al, 2013; Aranbarri et al., 2014; García-Prieto, 2015). VIL sequence (Figure1) extends back to the Termination II and thus, constitutes a reference site for Southern Europe paleoclimate and paleoenvironmental variations covering the last two glacial cycles. Here we present and discuss the multidisciplinary dating approach (including radiocarbon, U/Th, paleomagnetism, OSL, IRSL and tephrochronology) used for the development of the best possible age model in VIL sequence for the last ca. 135 ka and discuss the main benchmarks used to produce such a model that might be useful for other similar long sequences. We explore the coherency of this age model against the available sedimentological data, preliminary selected pollen results, and other records from mid-latitudes.

2. REGIONAL SETTING

2.1. The Jiloca Basin

The ‘El Cañizar de Villarquemado’ wetland is located in the Iberian Range, Northeastern Spain (Figure 1A), at ca. 1000 m a.s.l., in the southernmost area of the 60 km long Jiloca Depression, an Upper Pliocene N-S half-graben bounded by NW-SE trending normal faults (Rubio and Simón, 2007**)**. During the Quaternary, the northern areas of the Jiloca Basin changed to exorheic drainage progressively while in the southern area endorheic conditions remained (Gutiérrez-Elorza and Gracia, 1997) and a shallow (up to 2.8 m deep) lake developed, covering a maximum surface area of 11.3 km^2 (Figure 1B) and becoming the largest freshwater lake in the Iberian Range and one of the largest in the Iberian Peninsula (Rubio, 2004). The lake was drained to the north during the 18th century to increase agricultural land and reduce flooded areas perceived as a source of mosquito-borne diseases (Rubio, 2004). The evolution of the lake basin has been controlled by tectonics, subsidence, and the depositional dynamics of two ephemeral streams to the north, the Villarrosano and Rebollos. As the basin sits on Mesozoic limestones, variable karstic activity during the last millennia could also have affected base level and influenced depositional history (Gracia et al., 2003; Gutiérrez et al., 2008, 2012).

Current regional vegetation plant communities are mainly composed by oaks (*Quercus ilex rotundifolia, Q. faginea*), junipers (*Juniperus thurifera, J. phoenicea*), and pines (*Pinus nigra, P. pinaster* and *P. sylvestris*) as the dominant trees, depending on altitude, exposure and soil type. Open Mediterranean xerophytic shrub communities with *Rhamnus alaternus, Genista scorpius, Ephedra fragilis, Thymus* spp., *Rosmarinus officinalis* and *Artemisia assoana* amongst others are also frequent. The wetland surroundings are mostly cultivars. The climate of the region is Continental Mediterranean with long cold winters, hot summers, and a large water deficit (López-Martín et al., 2007).

2.2. The Cañizar de Villarquemado sediment (VIL) sequence

After an exploratory Livingstone extraction of ca. 2 m core length (VIL05-1A-1L), a 74 m long core was recovered in 2005 with a truck–mounted drill rig in the central area of the wetland (VIL05-1B-1T), where the basin depocenter was located (987 m a.s.l, 40°30’N; 1°18’W). The sediment cores were split lengthwise in two halves and imaged with a GEOTEK camera. High-resolution magnetic susceptibility profiles were acquired with a GEOTEK multisensory at the Limnological Research Center, University of Minnesota. Total Organic Carbon (TOC), Total Inorganic Carbon (TIC) and Total Nitrogen (TN) measurement were performed in samples taken at 2 cm intervals. XRF scanner measurements were performed every 4 cm with the ITRAX XRF at the Large

Lakes Observatory, University of Minnesota. Cores were correlated based on key markers, facies and geochemical profiles.

Twenty facies were identified and described based on sediment composition, textures, color and microscopic observations of smear slides following Schnurrenberger et al. (2003). They correspond to four textural types (sand, coarse silt, fine silt, organic-rich) (Table 1 and Figure 2) and have been grouped in four facies associations based on their depositional environments (FA): carbonate lake (A), clastic lake (B), wetland (C) and alluvial (D) (described previously in Moreno et al., 2012; González-Sampériz et al., 2013). VIL sequence exemplifies the characteristic large spatial and temporal variability of facies in shallow lacustrine basins (Cohen, 2003; Valero-Garcés et al., 2011, 2014). In this setting, a variety of sub-environments occur from distal alluvial fans (FA D), shallow carbonate ponds with charophyte meadows (FA A), areas with dominant organic deposition (FA C), and other with higher clastic input from the ephemeral or permanent inlets (FA B). Small changes in the hydrology, base level or accommodation space in the basin cause a lateral migration of the sub-environments. Development of a carbonate lake represents higher lake levels than during wetland/peatland stages while alluvial fans prograded over the lake basin during the lowest lake levels phases. Although bathymetric inferences from sediment composition are not straightforward in these settings, clastic lake facies are interpreted as relatively deeper deposition compared to carbonate lake facies as they require higher sediment and water input from the catchment area along small streams and creeks (Valero-Garcés et al., 2014). Equivalent modern examples of these lake environments are the Everglades in Florida (USA) or the Ruidera Lakes in Spain. Many examples occur during the Quaternary, in the early stages of large basins as the Great Salt Lake (Balch et al., 2005) and Titicaca (Fritz et al., 2007).

Seven sedimentary units have been defined in the sequence based on the occurrence of facies association (Figure 2): Unit VII (74–56m depth) groups facies from a depositional environment characterized as a mosaic of wetlands, peatlands and carbonate lakes with high carbonate production; Unit VI (56–38m depth), contains facies association B (clastic lakes) and C (wetlands); Unit V (38-29m depth) is characterized by the retreat of the wetlands and the pro-gradation of the alluvial fans over the distal areas of the lake basin (FA D and B); Unit IV (29-21m depth) is dominated by distal alluvial fan and mud flat environments (FA D); Unit III (21–15m depth) encompasses clastic lake (FA D) and distal alluvial fan facies (FA C); Unit II (15–3m depth) contains both, clastic and carbonate lake facies associations (A and B); and finally, Unit I (3-0m depth) represents a carbonate lake (FA A) with minor development of wetland/peatland environments (FA C).

3. METHODS: A MULTI-DATING TECHNIQUE STRATEGY FOR AN AGE MODEL

We have applied a number of dating techniques to VIL sequence, in order to obtain the best possible independent age model: radiocarbon, U/Th series, OSL, IRSL, paleomagnetism, and (crypto-) tephrochronology (Figure 2). In the next section we describe for every methodology the sampling procedures (sample numbers, selection criteria, etc.,) and the dating technique (chemical procedures, equipment, etc.).

3.1. Radiocarbon (AMS ^{14}C)

A total of twenty three AMS radiocarbon ages were obtained for VIL sequence (Table 2), twenty of them in the long core VIL05-1B-1T and three from the shorter parallel core VIL05-1A-1L (Aranbarri et al., 2014). Sediment samples were collected as 1 cm-thick sediment slices after detailed macroscopic descriptions and microscopic observation of smear slides to check for terrestrial remains. However, due to the absence of organic terrestrial macro-remains, all the analysed samples correspond to bulk sediment from intervals with high TOC content. Samples were analysed at Poznan Radiocarbon (Poland) and Beta Analytic (USA) laboratories and ages converted into calendar years using the INTCAL13 calibration curve (Reimer et al., 2013).

3.2. U/Th

Eleven samples were selected to run U/Th analyses (Table 3A). Firstly, we looked for pure endogenic inorganic carbonates, but the only occurrence were small carbonate coatings of aquatic plants and *Chara* fragments. We also selected well-preserved gastropods, although U uptake or loss in biological material poses challenges to dating (Bischoff and Cummins, 2001; Placzek et al., 2006a). Unfortunately, the number of gastropods or biological carbonate coating pieces at discrete levels was never enough to reach the minimum weight (ca. 100 mg) necessary for reliable U/Th analysis by ICP-MS in samples with relatively low U content, and consequently samples from several depths were combined (Table 3). Both biogenic coating carbonate particles and gastropods were cleaned by physically removing any adhered detritus. Samples were then treated with 6% NaOCl for 18–24 hr at room temperature to remove all organic material and then washed repeatedly in “ultrapure” water, sonicated for a few minutes to remove adhered solution, washed again, and dried in a vacuum oven overnight at ~70 ºC. The chemical procedure used to separate the uranium and thorium was carried out at the University of Minnesota (USA) laboratories following standard methodologies (Edwards et al., 1987; Cheng et al., 2013). Analyses were conducted by inductively coupled plasma mass spectrometry (ICP-MS) on a Finnigan-MAT Element outfitted with a double focusing sector-field magnet in reversed Nier–Johnson geometry and a single MasCom multiplier from the University of Minnesota laboratories.

3.3. Tephrochronology

To our knowledge VIL was one of the first records from NE Spain tested for cryptotephras. Based on a preliminary chronology (Moreno et al., 2012), the 4–24 m depth interval corresponded to ca. 159-50 ka was sampled contiguously and analysed for cryptotephra content. Facies sampled included clay and silt beds with some interspersed fine sandy layers. Numerous techniques have been employed to detect cryptotephra within sedimentary records. These techniques utilise both direct (e.g. extraction of volcanic glass) and indirect (e.g. magnetic signals) approaches. Here the method proposed by Turney et al. (1997), Turney (1998) and Blockley et al. (2005) was employed, involving a stepped density separation using the inert heavy liquid sodium polytungstate (SPT). Firstly a 'cleaning' float (specific gravity of 1.98 g cm^{-3}) is performed to remove organics and diatoms, and then an 'extraction' float (specific gravity of 2.55 g cm^{-3}) is carried out to separate the tephra shards from the heavier minerogenic material. The published methods are deliberately flexible, allowing the analysed grain-size and the separation densities to be tailored to the host sediment type and expected volcanic ash characteristics. We chose to follow the recommended separation densities, which have been carefully tested by Blockley et al. (2005) to show optimal extraction of the majority of tephra shards encountered within several European volcanic sources (e.g. Icelandic, Italian and Eifel). If present in the VIL core, basaltic glass shards with a higher specific gravity than the SPT extraction density, were not lost, but retained in residues for inspection after the main float was counted. We chose to analyse the sediment fraction between 125µm and 15µm. This is a wider size range than the 80 - 25µm fraction most commonly used for cryptotephra (Blockley et al., 2005), reflecting the uncertainty about the volcanic sources able to transport tephra to NE Iberia. Smaller grain-size fractions are commonly used to maximise shard numbers in this way (e.g. Kuehn and Froese, 2010), particularly where sites are very distal from volcanic sources and their typical dispersal axes.

3.4. Single –grain OSL and infrared stimulated luminescence (IRSL)

Fourteen luminescence dating samples were collected from unopened sections of VIL core and from some previously opened sections that had remained wrapped and stored in a cold room since field recovery (Tables 4 and 5). Two luminescence dating techniques have been used on these samples: i) five samples were dated using traditional multi-grain aliquot infrared stimulated luminescence (IRSL) at the Universidad Autónoma de Madrid's commercial dating laboratory, and ii) nine samples were dated using single-grain OSL at the CENIEH laboratories (Burgos, Spain). The results of the IRSL study have been already published (Moreno et al., 2012; González-Sampériz et al., 2013) and are only summarised briefly in the current study. The single-grain results were obtained by our own research team as part of the present dating study, and are presented for the first time here. In both cases, the most homogeneous silt or sand-sized layers were sampled in order to minimise uncertainties in gamma dose rate estimation. Blocks of 5-15 cm vertical length were cut from 60 cm-long core sections using a knife and wrapped in light-proof bags for transportation. Coarse-grained (212-250 µm or 180-250 µm) quartz and fine-grained (2-10 µm) polymineral fractions were prepared for OSL and IRSL burial dose estimation, respectively, using standard procedures (Aitken, 1998). A 48% (40 min) hydrofluoric acid etch was used to remove the alpha-irradiated external layers of the sand-sized quartz grains.

Multi-grain aliquot IRSL measurements were made using a Risø TL-DA-10 reader equipped with IR LEDs and a calibrated $^{90}Sr/^{90}Y$ beta source. Further procedure details of these previously published results are given in the Appendix.

For the single-grain OSL dating approach, equivalent dose (D_e) values were estimated from the ultraviolet emissions of individual grains of quartz using the same instrumentation, single-aliquot regenerative-dose (SAR) protocol (Murray and Wintle, 2000), and associated grain rejection criteria described in Arnold et al. (2012, 2013). Single grains were optically stimulated using a focussed 10 mW green (532 nm) laser for 2 s at 125°C. Sensitivity-corrected dose-response curves were constructed using the first 0.08 s of each green laser stimulation after subtracting a mean background count obtained from the last 0.25 s of the OSL signal. D_e uncertainties were derived from net photon counting statistics, an empirically determined instrument reproducibility of 1.8% per OSL measurement (calculated for the Risø reader used in this study), and a dose-response curve-fitting uncertainty determined using 1000 iterations of the Monte Carlo method described by Duller (2007) (implemented in Analyst v3.24). A preheat of 200 ^{o}C for 10 s was used in the SAR procedure prior to measuring the natural- and regenerative-dose OSL signals. A preheat of 160 ^{o}C for 10 s was applied prior to each test dose OSL measurement. Single-grain dose-recovery tests performed on V127 yielded measured-to-given dose ratios consistent with unity (0.96 ± 0.03) and a relatively low over-dispersion value of 11 ± 4%, confirming the suitability of the chosen SAR conditions for single-grain D_e estimation.

Environmental dose rates were calculated for the single-grain OSL samples using high-resolution gamma spectrometry measurements made with high-purity Ge detectors (an n-type closed-end coaxial system and a p-type well system) (see SI for further details). To estimate the long-term water content of the single-grain OSL samples we have used the 'as measured' values and included a correction to account for progressive decreases in sediment porosity with time. This correction has been included because of the relatively thick sediment overburdens (27-73 m) affecting these samples and, hence, the increased likelihood of sediment compaction and dewatering effects with time (e.g., Rendell, 1985; Sheldon and Retallack, 2001; Olley et al., 2004a, Kadereit et al., 2012; Lukas et al., 2012; see Table 1 and SI for further details).

3.5. Paleomagnetism

Due to the fact that VIL core is not oriented, only the paleomagnetic inclination can be considered (not declination). In addition, it is expected that the paleomagnetic declination is similar for the samples of the same section if the calculated stable paleomagnetic component is primary; i.e., it is acquired at the time of deposition of the sediments (detrital remanence magnetization DRM). For the last normal chron (Bruhnes chron, ~780 ka, v) up to 5 excursions of the magnetic field occurred (Channell, 2006), and one of them – the Blake excursion ~120 ka - has been recently radiometrically dated in a Northern Spain speleothem between 112 and 116.5 ka (Osete et al., 2012). Consequently, to better constrain the basal age of VIL sequence, we focused the paleomagnetic study in the interval where the preliminary dating (Moreno et al., 2012) suggested the 120 ka horizon occurs. Thirty three samples were taken every 10 to 20 cm along the selected depth interval by cutting the half core with a ceramic knife in cubes of 2 cm. The analyses were carried out at the Paleomagnetism Laboratory of the University of Burgos, Spain. A 2-G cryogenic with automated alternating field demagnetization coils were used to measure the remanence and to carry out the stepwise demagnetization procedure, respectively. Three samples were thermally demagnetized but results were good in the AF demagnetization, therefore, the AF demagnetization procedure was preferred. The calculation of the paleomagnetic components was done with Remasoft (Chadima and Hrouda, 2009), which follows the principal component analyses of Kirschvink (1980).

4. RESULTS

4.1. Radiocarbon (AMS ^{14}C)

Seven of the twenty three AMS ages show reversal or outliers ages compared to the preceding and subsequent samples (in italics in Table 2). Three of them, at 135, 638.2 and 989.5 cm depth (VIL05-1B-1T) have relatively higher algal organic matter content as deduced from their relatively low TOC/TN ratios and $\delta^{13}C$ values (Table 2). This feature could explain their relatively "too old" ages, as they could be more affected by old carbon in the lake water reservoir. The other four ages are inconsistent with the general chronostratigraphy, but to make the decision on which radiocarbon dates were to be included in the final model we ran an initial Bayesian model (details explained in the Discussion section below) and these 7 ages were excluded. Therefore, the final radiocarbon model is constrained by 16 AMS ^{14}C ages for the upper 20 m of the composite sequence.

4.2. U/Th

A number of problems, common when dating lacustrine carbonates by U/Th (Placzek et al., 2006 a) were encountered in VIL sequence, and finally, only three samples produced ages (VIL-2, -3 and -4; Table 3B). Firstly, even after long procedures, the amount of suitable material collected was too small, thus leading to higher uncertainty in the results. Secondly, carbonate-coatings were more difficult to clean than gastropod samples, and even after a very careful cleaning, the ^{232}Th concentration in all samples was very high. The ^{230}Th/^{232}Th ratio is only above 100 for VIL-3 and VIL-4 (Table 3B). The high detrital content impeded the calculation of a meaningful age for samples VIL-1, VIL-5 and VIL-6 and produced a large associated uncertainty in sample VIL-2.

The uncertainties on the three dated samples (VIL-2, -3 and -4) are high, particularly for sample VIL-2, likely because of the high detrital content and the low sample weight. Potential variability in any assumed initial ^{230}Th/^{232}Th ratio is usually high in lacustrine samples because the proportion of ''siliciclastic Th'' and ''unsupported Th'' may not be constant (Placzek et al., 2006b). Therefore, age corrections using a constant initial ^{230}Th/^{232}Th ratio introduce larger errors, as reflected in the inaccuracies of the dated samples VIL-2, -3 and -4. Isochron techniques could probably help to obtain an age for these samples after initial ^{230}Th/^{232}Th ratio determination of the non-carbonated detritus. However, the requirement of obtaining multiple sub-samples with different degrees of contamination at the same core depth (same age) prevents the application of this methodology to VIL core, particularly as it was difficult collecting sufficient material for just one sample at each depth.

The uppermost age (VIL-2) was rejected because it has the largest error and it is also stratigraphically reversed compared to the other two ages (VIL-3 and VIL-4). Thus, although six samples (endogenic and biogenic carbonates) were prepared and analysed, only two biogenic samples (gastropods) could be considered valid samples. Since these two samples (VIL-3 and VIL-4) were obtained close to the base of the core they could provide a basal age for the sequence, although the ages were much older (240 ka in U-Th) compared to the IRSL dates (140 ka, see below). Biological effects were considered responsible for this discrepancy, as one prerequisite for U/Th dating is a chemically -closed radioactive system, and this is unfortunately rarely the case for biogenic carbonates with chemical U-mobility, particularly during early diagenetic stages (Placzeck et al., 2006a,b). Unfortunately, the absence of suitable material impeded the use of the U/Th series techniques to correctly date VIL sequence.

4.3. Tephrochronology

Cryptotephra studies from Europe and the North Atlantic have shown that small concentrations of volcanic ash can be found over several thousands of km away from their source (Lane et al., 2017), therefore we expected some volcanic ash in El Cañizar de Villarquemado. However, only a few tephra shards (<5 shards per gram) at two intervals (5.90-6.00 and 12.30-12.50 m depth) were detected under high powered optical microscopic analysis of the extracted residues within the depth interval 4-23m. Despite extensive efforts, however, these could not be replicated at higher 1 cm resolution and thus neither their integrity as primary ash fall layers could be confirmed nor geochemical analyses carried out (Figure 4). These results are similar to other recent attempts from paleo-archives across the Iberian Peninsula (Sanabria, Estanya; unpublished data) where no cryptotephra were detected or, samples yielded minimal evidence of tephra input and were insufficient for geochemical analysis.

Tephra occurrences in Late Quaternary Iberian records are rare and seem restricted to Early Holocene volcanic activity in La Garrotxa region, Northeastern Spain (Höbig et al., 2012; Bolòs et al., 2015). Volcanic ash could reach the Iberian Peninsula from several sources: the Azores islands to the west, the Iceland to the north and Massif Central and Italian volcanic systems to the East, all of which were active and generated far-travelled tephra deposits during the last glacial cycle.

The most likely reason that ash from northern and eastern volcanic sources did not reach Iberia is because the atmospheric circulation patterns were dominated by a strong westerly and Northwestern component during the Last Glacial (Moreno et al., 2005), as they are today (Barry and Chorley, 1992). This essentially blocks atmospheric transport paths required for transport of ash from East to far West. In fact, during the last 2010 Icelandic Eyjafallajökull volcano eruption (Stevenson et al., 2012), only small size volcanic particles were detected in Iberia (Revuelta et al., 2012) and no relevant ash particles deposited.

It is unclear why volcanic ash from the Azores volcanic system, located around 2000 km to the west of El Cañizar de Villarquemado and highly active during the Last Glacial with multiple caldera-forming eruptions (Moore, 1990) has not been found yet in any Iberian lake sequence. One aspect that deserves further studies is the role of precipitation and aridity in tephra deposition dynamics, as periods of higher aridity and varied vegetation cover during the Last Glacial Cycle in Iberia (García-Ruiz et al. 2003; González-Sampériz et al. 2010; 2017; Moreno et al., 2012; Sancho et al., 2018), may have significantly reduced the potential for tephra deposition and preservation.

Another possibility is that grain size of the volcanic particles reaching Iberia may be too small to have been detected with our techniques. Tephra grain size distributions distal to source are controlled by factors including the volume of material ejected during the explosive phase of an eruption, the timing and extent of magma fragmentation and processes of aeolian fractionation during atmospheric transport. Iberia lies several hundreds of km away from most explosive volcanic regions. The 2010 Eyjafallajökull eruption was less explosive than many Late Quaternary eruptions are believed to have been (Davies et al., 2010; Stevenson et al., 2015), however it provides evidence that some volcanic ash may reach Iberia, but only in very small quantities and size fractions. Within this investigation, 15µm was the smallest mesh size used, but if most tephra fall over Iberia falls within a much smaller particle size range, sieves with smaller mesh diameters may need to be employed in future cryptotephra investigations. This has non-trivial implications for both optically identifying tephra at these small sizes and acquiring geochemical data for characterisation: as the smallest electron microprobe beam size currently in use for glass analysis is 3µm (Haywood, 2012), whilst ~10 µm is more conventional (Kuehn et al., 2011).

Whilst cryptotephrochronology was not successful in VIL, it is clear that to establish the absence or presence of non-visible ash layers in other areas of Iberia, requires a more comprehensive assessment of a larger number of Late Quaternary sediment sequences.

4.4. Paleomagnetism

The paleomagnetic results are shown in Figure 3. Samples demagnetized below 90 mT. The natural remanent magnetization averages in 6.2 e-4 A/m with a standard deviation of 7.6e-4 A/m (Figure 5a). In 23 samples, two stable components can be calculated, one that demagnetized between 2 and 16 mT (3-7 steps), and the component that directs towards the origin (characteristic) and demagnetizes between 10-30 and 40-90 mT (4-19 steps) (Figures 4a to 4e). These two components can be calculated in the coarser facies (grey silts and brownish sands) but not in the black clays (Figure 4b). The viscous component groups in a northerly and normal component, probably due to acquisition of the present day magnetic field during storage. The characteristic component shows normal and reverse polarity in almost all sections (not in 103, 106 and 109 due to low number of samples), but the declination is not similar among the samples of the same section (or antipodal in the case of opposite polarity, Figure 4f). Therefore, a secondary stable remanent magnetization was acquired after deposition of the sediments, maybe during coring extraction. Diagenetic redox reactions may have also imprinted a secondary polarity as post-sedimentary magnetization can occur (Roberts, 2015 and references therein). This could have been the case for the black clays, with very low NRM and unstable paleomagnetic behaviour, due to the destruction of ferromagnetic minerals by redox reactions in more organic matter-rich sediments.

To sum up, paleomagnetic studies could not determine a consistent reverse polarity in the lower interval of the sequence that could be related to the Blake excursion (~120 ka).

4.5. OSL

Multi-grain aliquot IRSL results

The previously published IRSL ages for the five VIL samples are summarised in Table 4. The multi-grain aliquot IRSL ages are stratigraphically consistent and the age of sample MAD-5172SDA (40.4 ± 3.4 ka) is in good agreement with two bracketing AMS ^{14}C ages of 36.3-40.2 ka and 40.2-42.9 ka (Table 5). Multiple aliquot storage tests conducted on these samples suggest that the polymineral (feldspar dominated) IRSL signals are not significantly affected by anomalous fading. However, there are a number of practical difficulties associated with deriving reliable fading assessments using traditional (non-normalised) multiple aliquot additive dose procedures (Aitken, 1998). More rigorous, sensitivity-corrected SAR anomalous fading tests were not performed on these samples following the widely adopted procedures of Huntley and Lamothe (2001) and Auclair et al. (2003). As such, we cannot preclude the possibility of minor age underestimation arising from unaccounted fading with the multi-grain aliquot IRSL results. This cautionary interpretation seems particularly appropriate given the low preheat temperatures used for D_e estimation (180 ºC for 10 s) and the fact that ultraviolet rather than blue IRSL emissions were measured in the MAAD procedure (e.g., Clarke and Rendell, 1997; Preusser, 2003).

Single-grain OSL results

Table 5 and Figure 4 summarise the single-grain D_e estimates, dose rate data and final ages obtained for El Cañizar de Villarquemado samples. The specific activities of individual isotopes in the ^{238}U and ^{232}Th and ^{40}K series are also shown in Table 6. Isotopic ratios for $^{226}Ra/^{238}U$, $^{210}Pb/^{226}Ra$ and $^{228Th}/^{228}Ra$ are consistent with unity at 1σ or 2σ for all nine samples, indicating that the ^{238}U and ^{232}Th decay chains of these sediments are within analytical uncertainty of present-day equilibrium. To calculate the optical ages of these samples, we have assumed that present-day equilibrium in the ^{238}U and ^{232}Th decay chains has prevailed throughout the burial period.

Between 900 and 1300 individual quartz grains were measured per sample (Table 5) and 6-9% of these grains were considered suitable for D_e determination after applying the single-grain quality assurance criteria outlined in Arnold et al. (2013). The D_e distributions of these samples can be broadly grouped into two categories. Samples V67, V127, V135 and V148 display homogeneous single-grain D_e distributions, characterised by relatively limited D_e scatter (e.g., Figure 5b). These D_e datasets are consistent with a single dose population centred on the weighted mean De value and display relatively low over dispersion values of ~13-22% (Table 5). These overdispersion values are consistent with the average value of ~20% commonly reported for well-bleached samples that have not been affected by post-depositional mixing or significant beta-dose spatial heterogeneity (e.g., Olley et al., 2004a; Arnold and Roberts, 2009, Arnold et al., 2011). The overdispersion values of these samples also overlap at 2σ with the over-dispersion value obtained in the single-grain dose-recovery test (11 ± 4%). The consistency of these results suggests that intrinsic sources of D_e scatter captured by the dose-recovery test likely account for the natural D_e distribution characteristics of these four samples and that extrinsic D_e scatter is relatively unimportant. We have therefore estimated the final burial doses for these samples from their weighted mean De estimates, calculated using the central age model (CAM) of Galbraith et al. (1999).

Samples V49, V58, V99, V110, V117, display broader D_e ranges (e.g., Figure 5c) and a significant proportion of the individual D_e values are not consistent with the sample-averaged (CAM) burial dose estimates at 2σ. The overdispersion values for these samples range between 26% and 37% and do not overlap at 2σ with the corresponding overdispersion value obtained for either the single-grain dose-recovery test or the 'best-case scenario' natural D_e distribution observed in the VIL core (sample V127: overdispersion = 13 ± 3%), suggesting that dose dispersion originating from extrinsic, field-related sources is more significant. The radial plots also display distinct 'leading-edges' of low D_e values and / or elongated, asymmetric 'tails' of higher D_e values, as has been commonly reported for partially bleached single-grain D_e distributions (e.g., Olley et al., 1999; 2004a; Bailey and Arnold, 2006; Arnold et al., 2007, 2009). Taking into account these empirical D_e characteristics, the alluvial and sub-aqueous origin of these deposits, and the potentially limited transportation distances experienced prior to deposition in this closed basin, it seems feasible that the additional D_e scatter may be primarily attributable to insufficient bleaching at the time of deposition; though minor dose dispersion arising from other extrinsic sources of D_e scatter (e.g., beta dose heterogeneity) cannot necessarily be discounted. Post-depositional mixing is not thought to have contributed significantly to the D_e scatter of these samples because primary sedimentary structures and distinctive boundaries are preserved through the sampled region of the core profile. In light of these considerations, the burial doses of samples V49, V58, V99, V110 and V117 have been determined using the 4-parameter minimum age model (MAM-4) of Galbraith et al. (1999). Further support for this choice of age model comes from the accuracy of the MAM-4 OSL age obtained for V49 (49 ± 8 ka). This OSL age is consistent with the expected age range of Unit IV based on an overlying ^{14}C sample (40.2-42.9 ka) and lithostratigraphic correlations of these deposits with MIS 3 (57-29 ka; Lisiecki and Raymo, 2005; Moreno et al., 2012). In contrast, the CAM age for V49 (79 ± 8 ka) is significantly older than the expected age range of Unit IV, consistent with the interpretation that this sample was poorly bleached prior to deposition.

Multi-grain and Single-grain integration

The nine single-grain OSL ages are internally consistent and in correct stratigraphically order, providing additional support for our age model selection procedure. The single-grain OSL ages and multi-grain aliquot IRSL ages are also in broad agreement with each other at their 1σ or 2σ error ranges, and provide a stratigraphically consistent combined chronological dataset. This age agreement between multi-grain and single-grain methods is somewhat unexpected given that several of the single-grain samples show evidence of prominent extrinsic D_e scatter that appears likely to be related to partial bleaching. It is possible, therefore, that the apparent age agreement between the two scales of analysis may reflect the fortuitous interplay of compensatory systematic biases that have passed undetected in the multi-grain aliquot IRSL datasets (e.g., problems of anomalous fading or the presence of aberrant grain populations with unreliable luminescence properties that would routinely be rejected in single-grain analysis; Demuro et al., 2008, 2013; Arnold et al., 2012; or the absence of a suitable overburden compaction correction procedure in the previously published IRSL study).

There are signs of an emergent systematic deviation between the single-grain OSL ages and multi-grain aliquot IRSL ages over the lower 15 m of the core (between a depth range of 59-74 m), though the two chronological datasets remain statistically indistinguishable at 2σ. This deviation might again reflect compensatory multi-grain aliquot inaccuracies, since age underestimation caused by unaccounted anomalous fading is likely to exert a more dominant influence over compensatory age overestimation arising from partial bleaching for increasingly older samples. In the absence of more direct evidence, these potential complications and averaging effects remain large unconstrained for the multi-grain IRSL datasets. We therefore place greater confidence in the single-grain OSL ages for the final age-depth model because the luminescence characteristics of each grain have been individually evaluated, and only grains that are considered reliable contribute to the final age determination. The single-grain OSL ages have also been derived using more rigorous and up-to-date analytical procedures and are based on a more thorough consideration of long-term changes in sediment water contents.

5. DISCUSSION

5.1. A Bayesian approach for El Cañizar de Villarquemado Age-Depth Model

5.1.1. Previous chronologies

Since the 2005 core extraction, several attempts have been made at modelling a robust independent chronology for VIL sequence. The first model included nine AMS ^{14}C ages and five IRSL ages (Moreno et al., 2012). This age model was developed using linear interpolation between all of the radiocarbon and IRSL ages. The base of the sequence was established at ca. 120 ka, with large basal age errors (ca. 10 ka). The robustness of this age model was strengthened by the coherence between the AMS ^{14}C age at 1912 cm (40.2 – 42.9 ka) and the IRSL age at 1832 cm (40.4 ± 3.4 ka).

A second age model (González-Sampériz et al., 2013) added three more AMS ^{14}C ages (twelve in total) for the top 20 m depth and was constructed following Heegaard et al., (2005). The time resolution for the Holocene improved but remained similar for the previous intervals. According to this second model, the base reached 130 ka and the boundary between MIS 6 and MIS 5 was tentatively located at the base of sedimentary unit VII (74 m depth), while MIS 4 was identified in sedimentary unit V (37-29 m depth) and MIS 3 comprised sedimentary units IV, III and the main part of II (29-5.5 m depth). Sedimentary unit I (top 2.5 m) represented MIS 1. Aranbarri et al. (2014) included four new AMS ^{14}C ages (1 from the long core and three more from the parallel core VIL05-1A) for the Holocene age model.

5.1.2. A Bayesian approach

To build the definitive age model we could only use ages obtained from three of the different techniques originally employed: AMS radiocarbon, IRSL and OSL. As discussed earlier, the only available U/Th dates were too old, likely as the biogenic carbonate system did not remain chemically closed, and the paleomagnetic studies could not determine a consistent reverse polarity in the lower interval of the sequence that could be related to the Blake excursion (~120 ka).

Preliminary age models clearly showed a lack of linearity in the age-depth relationships (Moreno et al., 2012; González-Sampériz et al., 2013; Aranbarri et al., 2014). This is a common feature in terrestrial sequences, where, very often, calibrated radiocarbon ages exhibit irregular probability distributions. Thus, we decided to combine the sixteen AMS ^{14}C ages, the five previously published IRSL ages and the nine single-grain OSL ages into a new Bayesian modelling framework (Blockley et al., 2008; Ramsey, 2009; Blaauw and Christen, 2011; Hogg et al., 2011; Goring et al., 2012). The rationale behind this method implies building up a depositional model reflecting more realistic age-depth relationships. Of particular significance for lake sequences is the fact that the accumulation process can be modelled by considering that the deposition rate at every depth is a weighted average of the previous depths (Blaauw and Christen, 2011). We have used Bacon v. 2.2 (Blaauw and Christen, 2011) for modelling purposes, which additionally incorporates radiocarbon age calibration using the INTCAL13 curve (Reimer et al., 2013).

Bacon controls core accumulation rates using a gamma autoregressive semi-parametric model with an arbitrary number of subdivisions along the sediment. This implies adding some prior knowledge on the evolution and shape (α) of accumulation rates, which serves as a smoothness factor for the age series, followed by a self-adjusting Markov Chain Monte Carlo (MCMC) process in order to build up a robust-to-outliers age model. The latter involves an adaptive algorithm that learns about the modelled process to automatically tune the MCMC simulation (Blaauw and Christen, 2011). Thus, the model includes as a pre-requisite the known fact that different sections of a sequence have different accumulation rates. This means that low variation in the accumulation rates throughout the deposit implies a high "memory", or internal dependence amongst sections of the sequence. Therefore, this procedure demands the input of the mean accumulation rate expected (β) and the prior for the variability of accumulation rate, or "memory". Additionally, it is necessary to define the number of sections of the core in which the MCMC process will be repeated.

As in most long sequences, we lack precise *a priori* information on the accumulation rate of the sequence and, given the length of the sequence and the variability in sedimentary facies, building up a chronological model becomes challenging as the sedimentation rate will have certainly changed through the sequence. Therefore, to find the best set of priors to build the most suitable age-depth model for the VIL core, we carried out a sensitivity analysis (see Supplementary material for details on this method). From this analysis our parameters were set as follows: the number of divisions in VIL sequence was 30, which implies that the MCMC process is roughly renovated every 250 cm and that the variability of the sedimentation process is relatively high (memory strength = 1 and mean correlation of 0.5). We set our prior for the accumulation rate as a gamma distribution with shape 1 (α) and mean 30 (accumulation rate=30 yr cm^{-1}). The definitive age model for VIL (Figure 7) includes thus the 16 available AMS ^{14}C, IRSL and OSL ages, and considers the facies fluctuations along the sequence, especially the changes occurring between sedimentary units VI and V (38 m depth) and between sedimentary units V and IV (29 m depth).

According to this age model, we have identified the boundaries of the last 6 Marine Isotopic Stages (Shackleton et al., 2002; Lisiecki and Raymo, 2005; Rasmussen et al., 2014) in the VIL sequence at the following depths:

- End of MIS 6 (132.7-130 ka), 74-72.3 m depth interval.
- MIS 5 (130-71 ka), between 72.3-38.3 m depth.
- MIS 4 (71-57 ka), 38.3 -29.2 m depth.
- MIS 3 (57-29 ka), 29.2-9.9 m depth.
- MIS 2 (29-14 ka), 9.9-3 m depth.
- MIS 1(14 ka – current times), upper 3 m depth.

Figure 5 shows the age – depth model for the VIL sequence. Sedimentation rates were higher during cooler periods (end of MIS 6, MIS 5d, MIS5 b, MIS 4, MIS 2 onset and LGM) but also during MIS 3 when alluvial fans prograded into the lake basin and a more open landscape perhaps also contributed to greater sediment input (Fig. Sed. Rate changes, Appendix). On the contrary, during warm periods such as the Holocene and MIS 5e, the sedimentation rate was much lower since it is dominated by autochthonous processes (eg. carbonate productivity in the lake) and a smaller amount of sediment delivery from the catchment.

5.2. The evolution of El Cañizar de Villarquemado Lake basin during the last 135,000 years

The new age model allows increases the reliability of the timing for the main environmental and hydrological changes identified in the VIL sequence (Figure 6). Sedimentological, geochemical and palynological evolution identifies a number of large and rapid changes in the VIL basin during the last 135 ka. From a paleohydrological point of view, the development of carbonate lakes in the basin (facies association A in Figure 2, Table 1) represents periods of higher lake levels than during wetland stages, with higher TOC and lower MS. Alluvial fan deposits, with lower TOC content and higher MS, prograded during the periods with the lowest lake levels in the basin. Additionally, higher hydrophytes and hygrophytes fossil pollen content (aquatic taxa) as well as Pterydophyta spores (ferns), indicate periods of higher lake levels and/or wetlands development, thus, more local moisture conditions in the basin (Figure 6). Accordingly, increasing percentages in steppe taxa identify arid conditions and lowest lake levels, while fluctuations in the Mediterranean component group are representative of temperature variability.

The age–depth model corroborates that carbonate and peat-rich sediments (Figure 2, Table 1) were mainly deposited during the interglacials (Holocene and MIS 5), but also at the end of MIS 6, the beginning of MIS 4 and the second half of MIS 2 (Lateglacial). During these aforementioned phases we also find higher proportions of aquatic taxa pointing to increasing local moisture (Figure 6).

Presence of clastic lacustrine facies, low percentages of Mediterranean taxa and aquatics and increasing steppe taxa at the bottom of sedimentary unit VII (74 – 72 m depth, end of MIS 6 and beginning of MIS 5), suggest that the base of the sequence corresponds to relatively cool and drier climate conditions than afterwards. At a global scale, the age of Termination II is considered ca. 132-130 ka (Shackleton et al., 2002; Lisiecki and Raymo, 2005), although it has largely been a matter of debate (see literature review in Helmens 2014; Martrat et al., 2014; Sier et al., 2015). Similarly, the environmental responses were not synchronous over the European continent (i.e., Woillard and Mook, 1982; Guiot et al., 1989; Tzedakis et al., 1997, 2003; Kukla et al., 1997; Allen and Huntley, 2009).

Based on our age model, the MIS 6 – MIS 5 boundary (ca. 130 ka) is located at 72.3 m depth although it is at 70.3 m depth (ca. 127 ka) when the first carbonate lake was established (facies association A in Figure 2). The signature of interglacial conditions in VIL after the onset of MIS 5 (Figure 6) was characterized by a trend towards warmer conditions but still relatively low effective moisture, as reflected both in the sediment depositional and vegetation responses. This is indicated by the development of a shallow carbonate lake and the lowest proportions of local moisture vegetation formations within MIS 5 and highest values of steppe taxa (Figures 2 and 6).

Regarding the pollen data, a general decrease in steppe taxa is evidenced since ca. 127 ka (MIS 5e). In parallel, a development of local moisture indicators is recorded at the basin since ca. 125 ka. However the Mediterranean component presents the same values along the MIS 6 – MIS 5 boundary (González-Sampériz et al., 2013; García-Prieto, 2015).

Likewise, a similar palynological scenario has been identified for the Last Termination and the beginning of the Holocene (Aranbarri et al., 2014) where neither rapid changes nor clear shifts but similar palynological spectra regarding regional vegetation (mainly conifers and Mediterranean taxa) occur during first millennia (Figure 6). The absence of significant changes during Terminations in this record has been interpreted as a signature of the resilient character of vegetation in Mediterranean continental Iberia (González-Sampériz et al., 2013, 2017; Aranbarri et al., 2014; García-Prieto, 2015).

Detailed facies analyses of the MIS 5 interval - Units VII and VI in VIL, up to 38 m depth and until 70 ka - show seven major lacustrine carbonate - peat cycles covering the whole of MIS 5. The lacustrine facies are charophyte-rich sand and silt, banded to laminated grey silt, and variegated, bioturbated, mottled carbonate mud and silt (Table 1, Figure 2). Those cycles are well marked too by TOC rich intervals 1 to 7 (Figure 6). The three oldest cycles are dominated mainly by carbonated lake environments in the basin and would suggest deeper depositional conditions. This humid phase in our record would correspond with MIS 5e (ca. 127-112 ka, Figure 6) in agreement with the most humid period recorded in Monticchio between 127.2-109.5 ka and interpreted as the Eemian by Allen and Huntley, (2009). Consistently with the well-known warmer and moister climate conditions of the Eemian (Sánchez-Goñi et al., 1999, 2000, 2005; Tzedakis et al., 2001), the higher development of carbonate-rich facies in VIL sequence at this moment would suggest a warmer and more humid Eemian than the Holocene in this region too (Aranbarri et al., 2014; Garcia-Prieto, 2015), as has been reconstructed in most mid latitude areas (van Andel and Tzedakis 1996; Magri and Tzedakis, 2000; Andersen et al., 2004; Dahl-Jensen et al., 2013; Lunt et al., 2013; Otto-Bliesner et al., 2013; Bakker et al., 2014).

The second half of MIS 5 is characterized by a larger development of wetlands and less frequent carbonate lake environments, illustrating a trend towards relatively lower humidity (Figure 2), although pollen indicators show a similar composition of main vegetation groups including large local moisture fluctuations (Figure 6). Besides the three oldest TOC rich intervals corresponding with MIS 5e, we can observe one during MIS 5c (interval number 4) and the last three (5, 6 and 7: Figure 6) during MIS 5a. Similarly, higher proportions of Mediterranean taxa are also recorded in interstadials MIS 5c and MIS 5a, and interglacial MIS 5e, pointing to higher temperatures (Figure 6). The onset of Unit V (38.3 m, 71 ka) witnessed a significant depositional change in the basin, as wetlands started to recede while distal alluvial fans prograded over the central areas of the basin. The Mediterranean taxa disappeared, suggesting colder climate conditions but local moisture pollen indicators still record moderate values (Figure 6). Our age model dates this transition as the onset of MIS 4 (71 ka, Lisiecki and Raymo, 2005). At a regional scale (NE Iberian Peninsula), the transition from MIS 5 to MIS 4 was marked by colder conditions but humidity remained relatively high (González-Sampériz et al., 2010 and references therein), favouring the maximum glacier extension in the northern Iberian mountains (Lewis et al., 2009; Sancho et al., 2018).

In VIL sequence, the aridity trend that had started during MIS 4 reached a maximum during the lower part of MIS 3 (Unit IV, 21-29 m depth, ca. 57-44 ka). During this unit, there is clear evidence for the lowest paleohydrological levels in the basin in the form of red, oxidized, fine silt facies with pedogenic features (facies association D in Figure 2, Table 1). Strong arid conditions during the whole of MIS 3 (sedimentary units V, IV, III and the bottom part of unit II: ca. 57-29 ka) are indicated by the highest steppe taxa proportions and the lowest local moisture group percentages of the whole record (Figure 6). Besides, two of the four intervals with low pollen productivity or sterility recorded in VIL sequence (marked by shaded grey bands in Figure 6) are located in MIS

3, from ca. 50-43 ka and 37-31 ka, and they are the result of low pollen preservation conditions suggesting subaerial exposure.

MIS 2 and the Lateglacial (ca. 29-11.7 ka, 9.9-3 m depth) are characterized by greater environmental and climate variability as indicated by the diversity of sedimentary facies (Figure 2). Clastic-dominated lakes and alluvial fans covered the VIL basin, but evidence for subaerial exposure is not found during the first half of MIS 2 (Table 1 and Figure 2). The LGM is characterized by another new low pollen productivity interval between 4 and 5.5 m depth (ca. 22-16 ka following our age model: Figure 6). Deposition of clastic and carbonate silt facies during the Lateglacial suggest an increase in flooded area in the VIL basin and higher run off and sediment delivery. Steppe taxa decreased and never again reached similar proportions to those of MIS 3. Inversely, the aquatic taxa (local moisture group) developed, reaching the maximum values of the whole sequence during the Lateglacial (Figure 6). The Mediterranean component slowly expands and only peaks after the first millennia of the Holocene (Aranbarri et al., 2014).

The Holocene onset at 11.7 ka was abrupt from a sedimentological point of view, with the development of a carbonate lake (Figure 2) while terrestrial vegetation remained resilient with no significant changes until ca. 9.5 ka (Aranbarri et al., 2014), as observed in other inner Mediterranean regional sequences (González-Sampériz et al., 2017; Morellón et al., 2018 and references therein). Both pollen and sedimentological facies indicate that the most humid Holocene phase occurred between ca. 7.7-5 ka and was characterized by the highest development of carbonate facies (Figure 2, Table 1), the maximum spread of mesophytes, the expansion of mixed Mediterranean oak woodlands with evergreen *Quercus* as dominant forest communities, and more frequent higher lake level periods (Aranbarri et al., 2014). The return of shallow, carbonate-wetland environments occur in conjunction with a decrease of mesophytes (Aranbarri et al., 2014), consistent with the widely identified increasing aridity of the Late Holocene in the Western Mediterranean (Jalut et al., 2009; Di Rita et al., 2018).

6. CONCLUSIONS

A multi-technique dating approach was implemented for the 72 m long VIL sequence, including AMS radiocarbon, IRSL and OSL, U/Th, tephrochronology and paleomagnetism. In spite of the negative results of some techniques, this type of strategy is essential to maximize the chances of obtaining robust age models in terrestrial sequences. The final Bayesian age model for VIL sequence includes 16 AMS ^{14}C age, 5 previously published IRSL ages and 9 single-grain OSL ages, as adequate material was not found for some analyses (U/Th, tephrochronology) and other techniques did not provide reliable results (paleomagnetism). The Bayesian approach improved the accuracy and resolution of the age-depth model by incorporating additional information related to changes in accumulation rate, as revealed by detailed sedimentological analyses. The age model demonstrates large paleohydrological and vegetation variability since the penultimate Termination, which is consistent with main global climatic trends, despite some local idiosyncrasies. Shallow carbonate lake and wetland environments developed during the interglacials (Holocene and MIS 5), but also at the end of MIS 6, the beginning of MIS 4 and the second half of MIS 2 (Lateglacial). Clastic lakes dominated during MIS 2 and MIS 4, and distal alluvial fans prograded over the basin during MIS 3. Sedimentological, geochemical and palynological data suggest that the Eemian was wetter and warmer than the Holocene.

The onset of MIS 4 (71 ka) was marked by cooler conditions, although humidity remained relatively present until MIS 3, the most arid interval in the whole sequence. MIS 2 shows large depositional and vegetation variability. The Holocene onset was marked by an abrupt paleohydrological change, but the main terrestrial vegetation change was delayed up until 9.5 ka. This depositional and paleohydrological evolution of VIL lake during the last interglacial – glacial transition reveals higher moisture variability than expected, an abrupt inception of the last glacial cycle and a resilient response of vegetation in Mediterranean continental Iberia in both Terminations.

ACKNOWLEDGEMENTS

Funding for El Cañizar de Villarquemado sequence research has been provided by DINAMO (CGL-BOS 2009–07992), DINAMO2 (CGL-BOS 2012–33063), DINAMO 3 (CGL2015-69160-R) IBERIANPALEOFLORA (CGL-BOS 2012–31717) and GRACCIE-CONSOLIDER (CSD2007-00067) projects, provided by the Spanish Inter-Ministry Commission of Science and Technology (CICYT) and by the Aragon Government (DGA project, 2005-2006). Tephrochronology research was supported by the UK Natural Environment Research Council consortium RESET (NE/E015670/1). The single-grain OSL dating research was supported by Australian Research Council (ARC) Future Fellowship project FT130100195 and Discovery Early Career Researcher Award DE160100743. The work of BMB was supported by the IGNEX project (249894), funded by the FRIMEDBIO program of The Research Council of Norway. Graciela Gil-Romera is funded by the DFG funded project FOR 2358 "Mountain Exile Hypothesis".

DATA AVAILABILITY

Data for this research are available in Mendeley Data Repository

REFERENCES

Aitken, M. J., 1985. Thermoluminescence Dating. Academic Press, London, 359 p.

Aitken, M.J., 1998. An Introduction to Optical Dating: The Dating of Quaternary Sediments by the Use of Photon-Stimulated Luminescence. Oxford University Press, Oxford, 267 p.

Allen, J.R.M., Huntley, B., 2009. Last Interglacial palaeovegetation, palaeoenvironments and chronology: a new record from Lago Grande di Monticchio, southern Italy. Quaternary Science Reviews 28, 1521-1538.

Andersen, K.K., Azuma, N., Barnola, J.M., Bigler, M., Biscaye, P., Caillon, N., Chappellaz, J., Clausen, H.B., Dahl-Jensen, D., Fischer, H. and Flückiger, J., 2004. High-resolution record of Northern Hemisphere climate extending into the last interglacial period. Nature 431, 147-151. Aranbarri, J., González-Sampériz, P., Valero-Garcés, B., Moreno, A., Gil-Romera, G., Sevilla-Callejo, M., García-Prieto, E., Di Rita, F., Mata, M.P., Morellón, M., Magri, D., Rodríguez-Lázaro, J., Carrión, J.S., 2014. Rapid climatic changes and resilient vegetation during the Lateglacial and Holocene in a continental region of south-western Europe. Global and Planetary Change 114, 50–65.

Arnold, L. J., Bailey, R. M., Tucker, G. E., 2007. Statistical treatment of fluvial dose distributions from southern Colorado arroyo deposits. Quaternary Geochronology 2, 162–167.

Arnold, L.J., Demuro, M., Navazo Ruiz, M., Benito-Calvo, A., Pérez-González, A., 2013. OSL dating of the Middle Palaeolithic Hotel California site, Sierra de Atapuerca, north-central Spain. Boreas 42, 285-305.

Arnold, L.J., Demuro, M., Navazo Ruiz., 2012. Empirical Insights into multi-grain averaging effects from ‘pseudo’ single-grain OSL measurements. Radiation Measurements 47, 652-658.

Arnold, L.J., Roberts, R.G., 2009. Stochastic modelling of multi-grain equivalent dose (D_e) distributions: Implications for OSL dating of sediment mixtures. Quaternary Geochronology 4, 204-230.

Arnold, L.J., Roberts, R.G., Galbraith, R.F., DeLong, S.B., 2009. A revised burial dose estimation procedure for optical dating of young and modern-age sediments. Quaternary Geochronology 4, 306-325.

Arnold, L.J., Roberts, R.G., MacPhee, R.D.E., Haile, J.S., Brock, F., Möller, P., Froese, D.G., Tikhonov, A.N. Chivas, A.R., Gilbert, M.T.P., Willerslev, E., 2011. Paper II – Dirt, dates and DNA: OSL and radiocarbon chronologies of perennially-frozen sediments and their implications for sedimentary ancient DNA studies. Boreas 40, 417-445.

Arnold, L.J., Demuro, M., Parés, J.M., Pérez-González, A., Arsuaga, J.L., Bermúdez de Castro, J.M., Carbonell, E., 2015. Evaluating the suitability of extended-range luminescence dating techniques over Early and Middle Pleistocene timescales: published datasets and case studies from Atapuerca, Spain. Quaternary International 389, 167-190.

Athy, L.F., 1930. Density, porosity and compaction of sedimentary rocks. Bulletin of the American Association of Petroleum Geologists 14, 1-24.

Auclair, M., Lamothe, M., Huot, S., 2003. Measurement of anomalous fading for feldspar IRSL using SAR. Radiation Measurements 37, 487-492.

Bailey, R. M., Arnold, L. J., 2006. Statistical modelling of single grain quartz De distributions and an assessment of procedures for estimating burial dose. Quaternary Science Reviews 25, 2475–2502.

Bakker, P., Renssen, H., 2014. Last Interglacial model-data mismatch of thermal maximum temperatures partially explained. Climate of the Past 10, 1633-1644.

Balch, D., Cohen, A., Schnurrenberger, D., Haskell, B., Valero-Garces B., Beck, W., Cheng H., Edwards, L. 2005. Ecosystem and paleohydrological response to Quaternary climate change in the Bonneville Basin, Utah. Palaeogeography, Palaeoclimatology, Palaeoecology 221, 99– 122.

Barry, R.G., Chorley, R.J., 1992. Atmosphere, Weather and Climate. Routledge, London.

Bischoff JL, Cummins K., 2001. Wisconsin Glaciation of the Sierra Nevada (79,000–15,000 yr B.P.) as Recorded by Rock Flour in Sediments of Owens Lake, California. Quaternary Research 55, 14–24.

Blaauw, M., Christen, J.A., 2011. Flexible paleoclimate age-depth models using an autoregressive gamma process. Bayesian Analysis 6, 457–474. Blockley, S.P.E., Pyne-O'Donnell, S.D.F., Lowe, J.J., Matthews, I.P., Stone, A., Pollard, A.M., Turney, C.S.M., Molyneux, E.G., 2005. A new and less destructive laboratory procedure for the physical separation of distal glass tephra shards from sediments. Quaternary Science Reviews 24, 1952–1960.

Blockley, S.P.E., Lane, C.S., Lotter, A.F., Pollard, A.M., 2007. Evidence for the presence of the Vedde Ash in Central Europe. Quaternary Science Reviews 26, 25-28, 3030-3036.

Blockley, S.P.E., Ramsey, C.B., Pyle, D.M., 2008. Improved age modelling and high-precision age estimates of late Quaternary tephras, for accurate palaeoclimate reconstruction. Journal of Volcanology and Geothermal Research 177, 251-262.

Bowler, J.M., Johnston, H., Olley, J.M., Prescott, J.R., Roberts, R.G., Shawcross, W., Spooner, N.A., 2003. New ages for human occupation and climatic change at Lake Mungo, Australia. Nature 421, 837-840.

Bischoff, J.L., Cummins, K., 2001. Wisconsin Glaciation of the Sierra Nevada (79,000–15,000 yr B.P.) as Recorded by Rock Flour in Sediments of Owens Lake, California. Quaternary Research 55, 14–24.

Bolós, X., Martí, J., Becerril, L., Planagumà, LL., Grosse, P., Barde-Cabusson, S., 2015. Volcano-structural analysis of La Garrotxa Volcanic Field (NE Iberia): Implications for the plumbing system. Tectonophysics 642, 58-70.

Brauer, A., Allen, J.R.M., Mingram, J., Dulski, P., Wulf, S., Huntley, B., 2007a. Evidence for last interglacial chronology and environmental change from Southern Europe. PNAS 104, 450-455.

Brennan, B.J., 2003. Beta doses to spherical grains. Radiation Measurements 37, 299-303.

Broecker, W.S., 2000. Abrupt climate change: causal constraints provided by the paleoclimate record. Earth-Science Reviews 51, 137-154.Brown, E.T., Werne, J.P., Lozano-García, S., Caballero, M., Ortega-Guerrero, B., Cabral-Cano, E., Valero-Garces, B.L., Schwalb, A. and Arciniega-Ceballos, A., 2012. Scientific drilling in the basin of Mexico to evaluate climate history, hydrological resources, and seismic and volcanic hazards. Scientific Drilling 14, 72-75.

Carrión, J.S., Leroy, S., 2010. Iberian floras through time: land of diversity and survival. Review of Palaeobotany and Palynology 162, 227-230.

Chadima, M. and Hrouda, F., 2009. Remasoft 3.0 Paleomagnetic Data Browser and Analyzer. Agico. Inc., Czech Republic.

Channell, J.E.T., 2006. Late brunhes polarity excursions (mono lake, laschamp, iceland basin and pringle falls) recorded at odp site 919 (Irminger basin). Earth and Planetary Science Letters 244, 378-393.

Cheng, H., Edwards, L.R., Hoff, J., Gallup, C.D., Richards, D.A., Asmerom, Y., 2000. The half-lives of uranium-234 and thorium-230. Chemical Geology 169, 17–33.

Cheng, H., Lawrence Edwards, R., Shen, C.-C., Polyak, V.J., Asmerom, Y., Woodhead, J., Hellstrom, J., Wang, Y., Kong, X., Spötl, C., Wang, X., Calvin Alexander, E., 2013. Improvements in 230Th dating, 230Th and 234U half-life values, and U–Th isotopic measurements by multi-collector inductively coupled plasma mass spectrometry. Earth and Planetary Science Letters 371–372, 82–91.

Clarke, M.L., Rendell, H.M., 1997. Infra-red stimulated luminescence spectra of alkali feldspars. Radiation Measurements 27, 221 – 236.Cohen, A. 2003. Paleolimnology. The History and Evolution of Lake Systems. Oxford University Press. 528 p.

Dahl-Jensen, D., Albert, M.R., Aldahan, A., Azuma, N., Balslev-Clausen, D., Baumgartner, M., Berggren, A.M., Bigler, M., Binder, T., Blunier, T. and Bourgeois, J.C., 2013. Eemian interglacial reconstructed from a Greenland folded ice core. Nature, 493, 489-494.Davies, S.M., Larsen, G., Wastegård, S., Turney, C.S.M., Hall, V.A., Coyle, L., Thordarson, T., 2010. Widespread dispersal of

Icelandic tephra: how does the Eyjafjöll eruption of 2010 compare to past Icelandic events? Journal of Quaternary Science 25, 605–611.

de Beaulieu, J.-L., Reille, M., 1989. The transition from temperate phases to stadials in the long Upper Pleistocene sequence from Les Echets (France). Palaeogeography, Palaeoclimatology, Palaeoecology 72, 147-159.

Demuro, M., Roberts, R. G., Froese, D. G., Arnold, L. J., Brock, F., Bronk Ramsey, C., 2008. Optically stimulated luminescence dating of single and multiple grains of quartz from perennially frozen loess in western Yukon Territory, Canada: comparison with radiocarbon chronologies for the late Pleistocene Dawson tephra. Quaternary Geochronology 3, 346–364.

Demuro, M., Arnold, L.J., Froese, D.G., Roberts, R.G., 2013. OSL dating of loess deposits bracketing Sheep Creek tephra beds, northwest Canada: dim and problematic single-grain OSL characteristics and their effect on multi-grain age estimates. Quaternary Geochronology 15, 67-87.

Di Rita, F., Fletcher,W.J., Aranbarri, J., Margaritelli, G., Lirer, F., Magri, D., 2018. Holocene forest dynamics in central and western Mediterranean: periodicity, spatio-temporal patterns and climate influence. Scientific Reports 8, 8929.

Duller, G.A.T., 2007. Assessing the error on equivalent dose estimates derived from single aliquot regenerative dose measurements. Ancient TL 25, 15-24.

Edwards, R.L, Chen, J.H, Wasserburg, G.J., 1987. 238U-234U-230Th-232Th systematics and the precise measurements of time over the past 500.000 years. Earth and Planetary Science Letters 81, 175–192.

Fritz, S.C., Baker, P.A., Seltzer, G.O., Ballantyne, A., Tapia, P., Cheng, H., Edwards, R.L., 2007. Quaternary glaciation and hydrologic variation in the South American tropics as reconstructed from the Lake Titicaca drilling project. Quaternary Research 68, 410-420.

Galbraith, R.F., Roberts, R.G., Laslett, G.M., Yoshida, H., Olley, J.M., 1999. Optical dating of single and multiple grains of quartz from Jinmium rock shelter, northern Australia: Part I, experimental design and statistical models. Archaeometry 41, 339-364.

Gallagher, K., Lambeck, K. 1989. Subsidence, sedimentation and sea-level changes in the Eromanga Basin, Australia. Basin Research 2, 115-131.

García-Prieto, E., 2015. Dinámica paleoambiental durante los últimos 135.000 años en el Alto Jiloca: el registro lacustre de El Cañizar (PhD Thesis). Universidad de Zaragoza, Spain.

García-Ruiz, J. M., Valero-Garcés, B. L., Martí-Bono, C., González-Sampériz, P., 2003. Asynchroneity of maximum glacier advances in the central Spanish Pyrenees. Journal of Quaternary Science 18, 61-72.

García-Ruiz, J.M., López-Moreno, J.I., Vicente-Serrano, S., Lasanta-Martínez, T., Beguería, S., 2011. Mediterranean water resources in a global change scenario. Earth-Science Reviews 105, 121-139.

Giorgi, F., Lionello, P., 2008. Climate change projections for the Mediterranean region. Global and Planetary Change 63, 90-104.

González-Sampériz, P., Valero-Garcés, B.L., Moreno, A., Morellón, M., Navas, A., Machín, J., Delgado-Huertas, A. 2008. Vegetation changes and hydrological fluctuations in the Central Ebro Basin (NE Spain) since the Late Glacial period: saline lake records. Palaeogeography, Palaeoclimatology, Palaeoecology 259, 157-181.

González-Sampériz, P., Leroy, S.A.G., Carrión, J.S., Fernández, S., García-Antón, M., Gil-García, M.J., Uzquiano, P., Valero-Garcés, B., Figueiral, I., 2010. Steppes, savannahs, forests and phytodiversity reservoirs during the Pleistocene in the Iberian Peninsula. Review of Palaeobotany and Palynology 162, 427-457.

González-Sampériz, P., García-Prieto, E., Aranbarri, J., Valero-Garcés, B.L., Moreno, A., Gil-Romera, G., Sevilla-Callejo, M., Santos, L., Morellón, M., Mata, P., Andrade, A., Carrión, J.S., 2013. Reconstrucción paleoambiental del último ciclo glacial en la Iberia continental: la secuencia del Cañizar de Villarquemado (Teruel). Cuadernos de Investigación Geográfica 39, 49–76.

González-Sampériz, P., Aranbarri, J., Pérez-Sanz, A., Gil-Romera, G., Moreno, A., Leunda, M., Sevilla-Callejo, M., Corella, J.P., Morellón, M., Oliva, B., Valero-Garcés, B., 2017. Environmental and Climate Change in the Southern Central Pyrenees since the Last Glacial Maximum: a View from the Lake Records. Catena 149, 668-688.

Goring, S.J., Williams, J.W., Blois, J.L., Jackson, S.T., Paciorek, C.J., Booth, R.K., Marlon, J.R., Blaauw, M., Christen, J.A., 2012. Deposition times in the northeastern United States during the Holocene: establishing valid priors for Bayesian age models. Quaternary Science Reviews 48, 54-60.Gracia, F.J., Gutiérrez, F., Gutiérrez, M., 2003. The Jiloca karst polje-tectonic graben (Iberian Range, NE Spain). Geomorphology 52, 215–231.

Guérin, G., Mercier, N., Adamiec, G., 2011. Dose-rate conversion factors: update. Ancient TL 29, 5-8.

Guiot, J., Pons, A., deBeaulieu, J.L., Reille, M., 1989. A 140,000-year continental climate reconstruction from two European pollen records. Nature 338, 309–313.

Gutiérrez-Elorza, M., Gracia, F.J., 1997. Environmental interpretation and evolution of the Tertiary erosion surfaces in the Iberian Range (Spain). Geological Society, London, Special Publications 120, 147–158.

Gutiérrez, F., Gutiérrez-Elorza, M., Gracia, F.J., McCalpin, J.P., Lucha, P., Guerrero, J., 2008. Plio-Quaternary extensional seismotectonics and dreinage natural development in the central sector of the Iberian Chain (NE Spain). Geomorphology 102, 21-42.

Gutiérrez, F., Gracia, F.J., Gutiérrez, M., Lucha, P., Guerrero, J., Carbonel, D., Galve, J.P., 2012. A review on Quaternary tectonic and nontectonic faults in the central sector of the Iberian Chain, NE Spain. Journal of Iberian Geology 38 (1), 145–160.

Haywood, C., 2012. High spatial resolution electron probe microanalysis of tephras and melt inclusions without beam-induced chemical modification. The Holocene 22 (1), 119–125.

Heegaard, E., Birks, H.J.B., Telford, R.J., 2005. Relationships between calibrated ages and depth in stratigraphical sequences: an estimation procedure by mixed effect regression. The Holocene 15, 1-7.

Helmens, K.F., 2014. The last interglacial-glacial cycle (MIS 5-2) re-examined based on long proxy records from central and northern Europe. Quaternary Science Reviews 86, 115-123.

Höbig, N., Weber, M.E., Kehl, M., Weniger, G.-H., Julià, R., Melles, M., Fülöp, R.-H., Vogel, H., Reicherter, K., 2012. Lake Banyoles (northeastern Spain): A Last Glacial to Holocene multi-proxy study with regard to environmental variability and human occupation. Quaternary International 274, 205-218.

Hodell, D.A., Anselmetti, F.S., Ariztegui, D., Brenner, M., Curtis, J.H., Gilli, A., Grzesik, D.A., Guilderson, T.J., Mnller, A.D., Bush, M.B., Correa-Metrio, A., Escobar, J., Kutterolf, S., 2008. An 85-ka record of climate change in lowland Central America. Quaternary Science Reviews 27, 1152-1165. Hoek, W.Z., Yu, Z.C., Lowe, J.J., 2008. INTegration of Ice-core, MArine, and TErrestrial records (INTIMATE): refining the record of the Last Glacial-Interglacial Transition. Quaternary Science Reviews 27, 1-5.

Hogg, A., Palmer, J., Boswijk, G., Turney, C., 2011. High-precision radiocarbon measurements of tree-ring dated wood from New Zealand: 195 BC-AD 995. Radiocarbon 53 (3), 529-542.

Huntley, D. J., Lamothe, M., 2001. Ubiquity of anomalous fading in K-feldspars and the measurement and correction for it in optical dating. Canadian Journal of Earth Sciences 38, 1093-1106.

Jalut, G., Dedoubat, J.J., Fontugne, M., Otto, T., 2009. Holocene circum-Mediterranean vegetation changes: climate forcing and human impact. Quaternary International 200, 4-18.

Johnson, E.A., Murphy, T., Torreson, O.W., 1948. Pre-history of the Earth's magnetic field. Journal of Geophysical Research 53(4), 349-372.

Kadereit, A., DeWitt, R., Johnson, T.C., 2012. Luminescence properties and optically (post-IR blue-light) stimulated luminescence dating of limnic sediments from northern Lake Malawi – Chances and limitations. Quaternary Geochronology 10, 160-166.

Kirschvink, J.L., 1980. The least-squares line and plane and the analysis of paleomagnetic data. Geophysical Journal of the Royal Astronomical Society 62, 669-718.

Kuehn, S.C.,Froese, D.G., 2010. Tephra from Ice-A Simple Method to Routinely Mount, Polish, and Quantitatively Analyze Sparse Fine Particles. Microscopy and Microanalysis 16 (2), 218–225.

Kuehn, S.C., Froese, D.G., Shane, P.A.R., INTAV Intercomparison Participants., 2011. The INTAV intercomparison of electron-beam microanalysis of glass by tephrochronology laboratorios: Results and recommendations. Quaternary International 246 (1–2), 19–47.

Kukla, G., McManus, J.F., Rousseau, D.-D., Chuine, I., 1997. How long and stable was the Last Interglacial. Quaternary Science Reviews 16, 605–612.

Lane, C.S., Lowe, D.J., Blockley, S.P.E., Suzuki, T. and Smith, V.C., 2017. Advancing tephrochronology as a global dating tool: Applications in volcanology, archaeology, and palaeoclimatic research. Quaternary Geochronology 40, 1-7.

Lézine, A.M., von Grafenstein, U., Andersen, N., Belmecheri, S., Bordon, A., Caron, B., Cazet, J.P., Erlenkeuser, H., Fouache, E., Grenier, C., Huntsman-Mapila, P., Hureau-Mazaudier, D., Manelli, D., Mazaud, A., Robert, C., Sulpizio, R., Tiercelin, J.J., Zanchetta, G., Zeqollari, Z., 2010. Lake Ohrid, Albania, provides an exceptional multi-proxy record of environmental changes during thelast glacial–interglacial cycle. Palaeogeography, Palaeoclimatology, Palaeoecology 287, 116–127.

Lewis, C., McDonald, E., Sancho, C., Peña, J.L., Rhodes, E., 2009. Climatic implications of correlated Upper Pleistocene glacial and fluvial deposits on the Cinca and Gállego

Rivers (NE Spain) based on OSL dating and soil stratigraphy. Global and Planetary Change 67, 141-152.

Lisiecki, L. E., Raymo, M. E. 2005. A Pliocene-Pleistocene stack of 57 globally distributed benthic d18O records. Paleoceanography 20, PA2007.

Litt, T., Krastel, S., Sturm, M., Kipfer, R., Örcen, S., Heumann, G., Franz, S.O., Ülgen, U.B., Niessen, F., 2009. “PALEOVAN”, International Continental Scientific Drilling Program (ICDP): site survey results and perspectives. Quaternary Science Reviews 28, 1555-1567.

Lionello, P, Mallanotte-Rizzoli, P, and Boscolo, R. (ed). 2012. Mediterranean Climate Variability. Developments in Earth and Environmental Sciences, Elsevier, 421 p.

Lopez-Martín, F., Cabera, M., Cuadrat, J.M., 2007. Atlas Climático de Aragón. Departamento de Medio Ambiente, Gobierno de Aragón, Zaragoza.Lukas, S., Preusser, F., Anselmetti, F.S., Tinner, W., 2012. Testing the potential of luminescence dating of high-alpine lake sediments. Quaternary Geochronology 8, 23-32.

Lukas, S., Preusser, F., Anselmetti, F.S., Tinner, W., 2012. Testing the potential of luminescence dating of high-alpine lake sediments. Quaternary Geochronology 8, 23-32.

Lunt, D.J., Abe-Ouchi, A., Bakker, P., Berger, A., Braconnot, P., Charbit, S., Fischer, N., Herold, N., Jungclaus, J.H., Khon, V.C., Krebs-Kanzow, U., Langebroek, P.M., Lohmann, G., Nisancioglu, K.H., Otto-Bliesner, B.L., Park, W., Pfeiffer, M., Phipps, S.J., Prange, M., Rachmayani, R., Renssen, H., Rosenbloom, N., Schneider, B., Stone, E.J., Takahashi, K., Wei, W., Yin, Q., Zhang, Z.S., 2013. A multi-model assessment of Last Interglacial temperatures. Climate of the Past 9, 699-

717.Magri, D., Tzedakis, P.C., 2000. Orbital signatures and long-term vegetation patterns in the Mediterranean. Quaternary International 73-74, 69–78.

Magri, D., Di Rita, F., Aranbarri, J., Fletcher, W., González-Sampériz, P., 2017. Quaternary disappearance of tree taxa from Southern Europe: timing and trends. Quaternary Science Reviews 163, 23-55.

Martrat, B., Grimalt, J.O., Lopez-Martinez, C., Cacho, I., Sierro, F.J., Flores, J.A., Zahn, R., Canals, M., Curtis, J.A., Hodell, D.A., 2004. Abrupt temperature changes in the western Mediterranean over the past 250,000 years. Science 306, 1762-1765.

Mejdahl, V., 1979. Thermoluminescence dating: beta-dose attenuation in quartz grains. Archaeometry 21, 61-72.

Mejdahl, V., 1987. Internal radioactivity in quartz and feldspar grains. Ancient TL 5, 10-17.

Melles, M., Brigham-Grette, J., Minyuk, P.S., Nowaczyk, N.R., Wennrich, V., DeConto, R.M., Anderson, P.M., Andreev, A.A., Coletti, A., Cook, T.L., HaltiaHovi, E., Kukkonen, M., Lozhkin, A.V., Rosen, P., Tarasov, P., Vogel, H., Wagner, B., 2012. 2.8 million years of arctic climate change from Lake El'gygytgyn, NE Russia. Science 337 (6092), 315-320.

Moore, R.B., 1990. Volcanic geology and eruption frequency, São Miguel, Azores. Bulletin of Volcanology 52, 602–614.

Morellón, M., Aranbarri, J., Moreno, A., González-Sampériz, P., Valero-Garcés, B. L., 2018. Early Holocene humidity patterns in the Iberian Peninsula reconstructed from lake, pollen and speleothem records. Quaternary Science Reviews 181, 1-18.

Moreno, A., Cacho, I., Canals, M., Grimalt, J.O., Sanchez-Goni, F., Shackleton, N., Sierro, F.J., 2005. Links between marine and atmospheric processes oscillating on a millennial time-scale. A multi-proxy study of the last 50,000 yr from the Alboran Sea (Western Mediterranean Sea). Quaternary Science Reviews 24, 1623-1636.

Moreno, A., González-Sampériz, P., Morellón, M., Valero-Garcés, B.L., Fletcher, W.J., 2012. Northern Iberian abrupt climate change dynamics during the last glacial cycle: A view from lacustrine sediments. Quaternary Science Reviews 36, 139-153.

Murray, A.S., Wintle A.G., 2000. Luminescence dating of quartz using an improved single-aliquot regenerative-dose procedure. Radiation Measurements 32, 57-73.

Murray, A.S., Wintle, A.G., 2003. The single-aliquot regenerative dose protocol: potential for improvements and reliability. Radiation Measurements 37, 377-381.

Murray, A.S., Roberts, R.G., 1997. Determining the burial time of single grains of quartz using optically stimulated luminescence. Earth and Planetary Science Letters 152, 163–180.

Nambi, K.S.V., Aitken, M.J., 1986. Annual dose conversion factors for TL and ESR dating. Archaeometry 28, 202-205.

Olley, J.M., Caitcheon, G.G., Roberts, R.G., 1999. The origin of dose distribution in fluvial sediments, and the prospect of dating single grains from fluvial deposits using optically stimulated luminescence. Radiation Measurements 30, 207–217.

Olley, J.M., Pietsch, T., Roberts, R.G., 2004a. Optical dating of Holocene sediments from a variety of geomorphic settings using single grains of quartz. Geomorphology 60, 337–358.

Olley, J.M., De Deckker, P., Roberts, R.G., Fifieldd, L.K., Yoshida, H., Hancock, G., 2004b. Optical dating of deep-sea sediments using single grains of quartz: a comparison with radiocarbon. Sedimentary Geology 169, 175-189.

Ojala, A.E.K., Francus, P., Zolitschka, B., Besonen, M., Lamoureux, S.F., 2012. Characteristics of sedimentary varve chronologies e a review. Quaternary Science Reviews 43, 45-60.

Ogg, J.G., Ogg, G., Gradstein, F.M., 2016. A Concise Geologic Time Scale: 2016. Elsevier, 234 p.

Opdyke, N. D, Channel, J.E.T., 1996. Magnetic stratigraphy. International Geophysics Series. Academic Press 64, 346 p.

Osete, M.L., Martín-Chivelet, J., Rossi, C., Edwards, R.L., Egli, R., Muñoz-García, M.B., Wang, X., Pavón-Carrasco, F.J., Heller, F., 2012. The Blake geomagnetic excursion recorded in a radiometrically dated speleothem. Earth and Planetary Science Letters 353, 173-181.

Otto-Bliesner, B., Rosenbloom, N., Stone, E., McKay, N.P., Lunt, D.J., Brady, E.C., Overpeck, J.T., 2013. How warm was the Last Interglacial? New model-data comparisons. Philosophical transactions. Series A, Mathematical, physical, and engineering sciences 371, 20130097.Pérez-Mejías, C., Moreno, A., Sancho, C., Bartolomé, M., Stoll, H., Cacho, I., Cheng, H., Edwards, R.L., 2017. Abrupt climate changes during Termination III in Southern Europe. Proceedings of the National Academy of Sciences of the United States of America 114, 10047–10052.

Placzek C, Patchett PJ, Quade J, Wagner, J.D.M., 2006a. Strategies for successful U-Th dating of paleolake carbonates: An example from the Bolivian Altiplano. Geochemistry, Geophysics, Geosystems 7, Q05024.

Placzek, C., Quade, J., Patchett, P.J., 2006b. Geochronology and stratigraphy of late Pleistocene lake cycles on the southern Bolivian Altiplano: implications for causes of tropical climate change. Geological Society of America Bulletin 118, 515–532.

Prescott, J.R., Hutton, J.T., 1994. Cosmic ray contribution to dose rates for luminescence and ESR dating: Large depths and long-term time variations. Radiation Measurements 23, 497-500.

Preusser, F., 2003. IRSL dating of K-rich feldspars using the SAR protocol: comparison with independent age control. Ancient TL 21, 17–23.Ramsey, C.B., 2009. Bayesian analysis of radiocarbon dates. Radiocarbon 51 (1), 337-360.Rasmussen, S.O., Bigler, M., Blockley, S.P., Blunier, T., Buchardt, S.L., Clausen, H.B., Cvijanovic, I., Dahl-Jensen, D., Johnsen, S.J., Fischer, H., Gkinis, V., Guillevic, M., Hoek, W.Z., Lowe, J.J., Pedro, J.B., Popp, T., Seierstadt, I.K., Steffensen, J.P., Svensson, A.M., Vallelonga, P., Vinther, B.M., Walker, M.J.C., Wheatley, J.J., Winstrup, M., 2014. A stratigraphic framework for abrupt climate changes during the Last Glacial period based on three synchronized Greenland ice-core records: refining and extending the INTIMATE event stratigraphy. Quaternary Science Reviews 106, 14-28.

Rees-Jones, J., 1995. Optical dating of young sediments using fine-grain quartz. Ancient TL 13, 9-14.

Reille, M., de Beaulieu, J.-L., Svobodova, H., Andrieu-Ponel, V., Goeury, C., 2000. Pollen analytical biostratigraphy of the last five climatic cycles from a long continental sequence from the Velay region (Massif Central, France). Journal of Quaternary Science 15, 665-685.

Reimer, P.J., Baillie, M.G.L., Bard, E., Bayliss, A., Beck, J.W., Bertrand, C.J.H., Blackwell, P.G., Buck, C.E., Burr, G.S., Cutler, K.B., Damon, P.E., Edwards, R.L., Fairbanks, R.G., Friedrich, M., Guilderson, T.P., Hogg, A.G., Hughen, K.A., Kromer, B., McCormac, G., Manning, S., Bronk Ramsey, C., Reimer, R.W., Remmele, S., Southon, J.R., Stuiver, M., Talamo, S., Taylor, F.W., van der Plicht, J., Weyhenmeyer, C.E., 2004. IntCal04 terrestrial radiocarbon age calibration, 0-26 cal kyr . Radiocarbon 46 (3), 1029-1058.

Reimer, P.J., Baillie, M.G.L., Bard, E., Bayliss, A., Beck, J.W., Blackwell, P.G., Bronk Ramsey, C., Buck, C.E., Burr, G.S., Edwards, R.L., Friedrich, M., Grootes, P.M., Guilderson, T.P., Hajdas, I., Heaton, T.J., Hogg, A.G., Hughen, K.A., Kaiser, K.F., Kromer, B., McCormac, F.G., Manning, S.W., Reimer, R.W., Richards, D.A., Southon, J.R., Talamo, S., Turney, C.S.M., van der Plicht, J., Weyhenmeyer, C.E., 2009. IntCal09 and Marine09 radiocarbon age calibration curves, 0-50,000 years cal . Radiocarbon 51, 1111-1150

Reimer, P.J., Bard, E., Bayliss, A., Beck, J.W., Blackwell, P.G., Bronk Ramsey, C., Buck, C.E., Cheng, H., Edwards, R.L., Friedrich, M., Grootes, P.M., Guilderson, T.P., Haflidason, H., Hajdas, I., Hatte, C., Heaton, T.J., Hoffmann, D.L., Hogg, A.G., Hughen, K.A., Kaiser, K.F., Kromer, B., Manning, S.W., Niu, M., Reimer, R.W., Richards, D.A., Scott, E.M., Southon, J.R., Staff, R.A., Turney, C.S.M., van der Plicht, J., 2013. IntCal 13 and Marine 13 radiocarbon age calibration curves 0-50,000 years cal . Radiocarbon 55, 1869-1887.

Rendell, H.M., 1985. The precision of water content estimates in the thermoluminescence dating of loess from northern Pakistan. Nuclear Tracks and Radiation Measurements 10, 763-768.

RESET (RESponse of humans to abrupt Environmental Transitions). Website: http://c14.arch.ox.ac.uk/reset/embed.php?File=index.html

Revuelta, M.A., Sastre, M., Fernández, A.J., Martin, L., Gómez-Moreno, F.J., Artinano, B., Pujadas, M., Molero, F., 2012. Characterization of the Eyjafjallajökull volcanic plume over the Iberian Peninsula by lidar remote sensing and ground-level data collection. Atmospheric Environment 48, 46–55.

Roberts, A.P., 2015. Magnetic mineral diagenesis. Earth-science reviews, 151, 1-47.

Rodbell, D.T., Abbott, M.B., 2012. Workshop on Drilling of Lake Junin, Peru: Potential for Development of a Continuous Tropical Climate Record. Scientific Drilling 13, 58-60.

Rubio, J.C., 2004. Contexto hidrogeológico e histórico de los humedales del Cañizar. Consejo de la Protección de la Naturaleza de Aragón, Serie de Investigración, Zaragoza.

Rubio, J.C, Simon, J.L., 2007, Tectonic subsidence v, erosional lowering in a controversial intramontane depression: the Jiloca basin (Iberian Chain, Spain), Geological Magazine 144, 127-141.

Russell, J.M., Bijaksana, S., Vogel, H., Melles, M., Kallmeyer, J., Ariztegui, D., Crowe, S., Fajar, S., Hafidz, A., Haffner, D., Hasberg, A., Ivory, S., Kelly, C., King, J., Kirana, K., Morlock, M., Noren, A., O'Grady, R., Ordonez, L., Stevenson, J., von Rintelen, T., Vuillemin, A., Watkinson, I., Wattrus, N., Wicaksono, S., Wonik, T., Bauer, K., Deino, A., Friese, A., Henny, C., Imran, Marwoto, R., Ngkoimani, L.O., Nomosatryo, S., Safiuddin, L.O., Simister, R., Tamuntuan, G., 2016. The Towuti Drilling Project: paleoenvironments, biological evolution, and geomicrobiology of a tropical Pacific lake. Scientific Drilling 21, 29-40.

Sánchez-Goñi, M.F., Eynaud, F., Turon, J.L., Shackleton, N.J., 1999. High resolution palynological record off the Iberian margin: direct land–sea correlation for the last interglacial complex. Earth and Planetary Science Letters 171, 123-137.

Sánchez-Goñi, M.F., Turon, J.L., Eynaud, F., Gendreau, S., 2000. European climatic response to millenial-scale changes in the atmosphere-ocean system during the Last Glacial period. Quaternary Research 54, 394–403.

Sánchez-Goñi, M.F., Loutre, M.F., Crucifix, M., Peyron, O., Santos, L., Duprat, J., Malaizé, B., Turon, J.L., Peypouquet, J.P., 2005. Increasing vegetation and climate gradient in Western Europe over the Last Glacial Inception (122–110 ka): data-model comparison. Earth and Planetary Science Letters 231 (1–2), 111–130.

Sancho, C., Arenas, C., Pardo, G., Peña-Monné, J. L., Rhodes, E. J., Bartolomé, M., García-Ruiz, J.M., Martí-Bono, C., 2018. Glaciolacustrine deposits formed in an ice-dammed tributary valley in the south-central Pyrenees: new evidence for late Pleistocene climate. Sedimentary Geology 366, 47-66.

Schnurrenberger, D., Russell, J., Kelts, K., 2003. Classification of lacustrine sediments based on sedimentary components. Journal of Paleolimnology 29, 141–154.

Shackleton, N.J., Chapman, M., Sánchez-Goñi, M.F., Pailler, D., Lancelot, Y., 2002. The classic marine isotope substage 5e. Quaternary Research 58, 14–16.Sheldon, N.D., Retallack, G.J., 2001. Equation for compaction of paleosols due to burial. Geology 29, 247-250.

Shen, C.-C., Edwards, R.L., Cheng, H., Dorale, J.A., Thomas, R.B., Moran, S.B., Weinstein, S.E., Edmonds, H.N., 2002. Uranium and thorium isotopic concentration measurements by magnetic sector inductively coupled plasma mass spectrometry. Chemical Geology 185, 165–178. Sier, M.J., Peeters, J., Dekkers, M.J., Pares, J.M., Chang, L., Busschers, F.S.B., Cohen, K.M., Wallinga, J., Bunnik, F.P., Roebroeks, W., 2015. The Blake Event recorded near the Eemian Type locality e a diachronic onset of the Eemian in Europe. Quaternary Geochronology 28, 12-28. Stein, M., Ben-Avraham, Z., Goldstein, S., Agnon, A., Ariztegui, D., Brauer, A., Haug, G., Ito, E., Yasuda, Y., 2011. Deep drilling at the Dead Sea. Scientific Drilling 46-47.

Stevenson, J.A., Loughlin, S., Rae, C., Thordarson, T., Milodowski, A.E., Gilbert, J.S., Harangi, S., Lukács, R., Højgaard, B., Árting, U., Pyne-O'Donnell, S., MacLeod, A., Whitney, B., Cassidy, M., 2012. Distal deposition of tephra from the Eyjafjallajökull 2010 summit eruption. Journal of Geophysical Research 117, B00C10.

Stevenson, J.A., Millington, S.C., Beckett, F.M., Swindles, G.T., Thordarson, T., 2015. Big grains go far: understanding the discrepancy between tephrochronology and satellite infrared measurements of volcanic ash. Atmospheric Measurement Techniques 8, 2069-2091. Thorarinsson, S., 1967. The eruptions of Hekla in historical times. A tephrochronological study. The eruption of Hekla 1947-48. 1, 1-170.

Turney, C.S.M., 1998. Extraction of rhyolitic component of Vedde microtephra from minerogenic lake sediments. Journal of Paleolimnology 19 (2), 199–206.

Turney, C.S.M., Harkness, D.D., Lowe, J.J., 1997. The use of microtephra horizons to correlate Late-glacial lake sediment successions in Scotland. Journal of Quaternary Science 12 (6), 525–531.

Tzedakis, P.C., Andrieu, V., de Beaulieu, J.-L., Crowhurst, S., Follieri, M., Hooghiemstra, H., Magri, D., Reille, M., Sadori, L., Shackleton, N.J., Wijmstra, T.A., 1997.

Comparison of terrestrial and marine records of changing climate of the last 500,000 years. Earth and Planetary Science Letters 150, 171–176.

Tzedakis, P.C., Andrieu, V., Birks, H.J.B., de Beaulieu, J.-L., Crowhurst, S., Follieri, M., Hooghiemstra, H., Magri, D., Reille, M., Sadori, L., Shackleton, N.J., Wijmstra, T.A., 2001. Establishing a terrestrial chronological framework as a basis for biostratigraphical comparisons. Quaternary Science Reviews 20, 1583–1592.

Tzedakis, P.C., Frogley, M.R., Heaton, T.H.E., 2003. Last Interglacial conditions in southern Europe, evidence from Ioannina, northwest Greece. Global and Planetary Change 36, 157–170.

Tzedakis, P.C., Hooghiemstra, H., Pälike, H., 2006. The last 1.35 million years at Tenaghi Philippon, revised chronostratigraphy and long-term vegetation trends. Quaternary Science Reviews 25, 3416–3430.

Tzedakis, P.C., 2007. Seven ambiguities in the Mediterranean palaeoenvironmental narrative. Quaternary Science Reviews 26, 2042–2066.

Valero-Garcés, B., Moreno, A., 2011. Iberian lacustrine sediment records: responses to past and recent global changes in the Mediterranean region. Journal of Paleolimnology 46, 319–325.

Valero-Garcés, B., Morellón, M., Moreno, A., Corella, P., Martín-Puertas, C., Barreiro, F., Pérez, A., Giralt, S., Mata-Campo, M.P., 2014. The carbonate factory in karst lakes: sources, processes and depositional environments in Quaternary Iberian Lakes. Sedimentary Geology 299, 1–29.

Van Andel, T.H., Tzedakis, P.C., 1996. Paleolithic landscapes of Europe and environs, 150,000-25,000 years ago: an overview. Quaternary Science Reviews 15, 481-500.

Wang, Y.J., Cheng, H., Edwards, R.L., An, Z.S., Wu, J.Y., Shen, C.C., Dorale, J.A., 2001. A high-resolution absolute-dated Late Pleistocene monsoon record from Hulu Cave, China. Science 294, 2345–2348.Woillard, G.M., Mook, W.G., 1982. Carbon-14 dates at Grande Pile: correlation of land and sea chronologies. Science 215, 159–161.

Zanchetta, G., Sulpizio, R., Roberts, N., Cioni, R., Eastwood, W.J., Siani, G., Caron, B., Paterne, M., Santacroce, R., 2011. Tephrostratigraphy, chronology and climatic events of the Mediterranean basin during the Holocene: An overview. The Holocene 21 (1), 33 –52.

Zanchetta, G., Regattieri, E., Giaccio, B., Wagner, B., Sulpizio, R., Francke, A., Vogel, L.H., Sadori, L., Masi, A., Sinopoli, G., Lacey, J.H., Leng, M.L., Leicher, N., 2016. Aligning MIS5 proxy records from Lake Ohrid (FYROM) with independently dated Mediterranean archives: implications for core chronology. Biogeosciences 13, 2757-2768.

Zimmerman, D.W., 1972. Relative thermoluminescence effects of alpha- and beta-irradiation. Radiation Effects 14, 81-92.

Zolitschka, B., F. Anselmetti, D. Ariztegui, H. Corbella, P. Francus, A. Lücke, N.I. Maidana, C. Ohlendorf, F. Schäbitz, S. Wastegård, 2013. Environment and climate of the last 51,000 years – new insights from the Potrok Aike maar lake Sediment Archive Drilling project (PASADO). Quaternary Science Reviews 71, 1-12.

TABLES

Table 1. Facies, facies associations and depositional environments in VIL sequence.

Table 2. Radiocarbon dates for the VIL sequence. Thirteen rejected dates are indicated by italics.

Table 3. U/Th samples for the VIL sequence (A) and obtained results (B).

Table 4. Dose rate data, multi-grain aliquot additive dose equivalent doses (De) and polymineral fine-grain IRSL ages for the VIL samples.

Table 5. Dose rate data, single-grain equivalent doses (De) and quartz OSL ages for the VIL samples.

Table 6. High-resolution gamma spectrometry results and daughter-to-parent isotopic ratios for VIL single-grain OSL samples.

FIGURE CAPTIONS

Figure 1. A. Location of Cañizar de Villarquemado Basin. B. Map of the watershed and maximum surface area of the wetland prior to drainage.

Figure 2. Stratigraphy of VIL sequence: sedimentary facies and associations, units, depositional environments and location of samples for different dating methods.

Figure 3. a) number of samples and value of NRM in A/m. b to e): stepwise AF demagnetization for selected samples represented in a stereoplot, orthogonal diagram and decay of normalized NRM. Observe that only sample d is from a black clay, with unstable paleomagnetic behavior. The other three samples show two stable paleomagnetic components. 5.f) Stereographic projection of calculated components. Viscous represent all the components and in pink the average of all together. In the other stereoplots the characteristic component of all samples is represented and in red, the data from the same section (number on top of each steroplot) is highlighted.

Figure 4. Representative single-grain De distributions for the VIL OSL samples, shown as radial plots. a) Ratios of recovered-to-given dose obtained for individual quartz

grains of V127 in the SAR dose-recovery test. The grey shaded region on the radial plot is centred on the administered dose for each grain (sample average = 300 Gy). Individual De values that fall within the shaded region are consistent with the administered dose at 2σ. b) Example of a homogeneous De distribution with limited dose overdispersion, indicative of a sample that has been sufficiently bleached prior to deposition. Here, the grey band is centred on the weighted mean De values used to calculate the OSL age, which was estimated using the central age model of Galbraith et al. (1999). c) Example of a more scattered De distribution that is not well-represented by the weighted mean burial dose estimate. This sample is cautiously interpreted as being heterogeneously bleached prior to deposition and its burial dose estimate (indicated by the grey bands) has been derived using the minimum age model of Galbraith et al. (1999).

Figure 5. The Bayesian Age model for the VIL sequence with all the dates included (A) and the final result with the main sedimentation rate changes indicated (B).

Figure 6. Main geochemical and palynological data of VIL sequence plotted in age with both sedimentological units (on the left) and MIS periods (on the right) indicated. Chronological limits for MIS periods follow Lisiecki and Raymo (2005) and Rasmussen et al. (2014) while stadials and interstadials into MIS 5 chronology follow Martrat et al. (2004). Pollen groups are composed by the following taxa: Mediterranean includes evergreen *Quercus, Viburnum, Buxus,* Oleaceae, *Pistacia, Rhamnus, Myrtus,* Thymelaeaceae, *Arbutus unedo*, Cistaceae and *Helianthemum*. Steppe includes *Ephedra distachya* and *E. fragilis* types and Chenopodiaceae. Local moisture is formed by aquatics and Pterydophyta: Cyperaceae, Typhaceae, *Juncus, Sparganium, Thalictrum, Lythrum, Stratiotes, Utricularia*, *Ledum palustre, Ranunculus, Pedicularis, Myriophyllum, Lemna, Nymphaea, Nuphar, Potamogeton, Isoetes, Alisma, Callitriche, Asplenium*, Monolete, Trilete, *Polypodium, Botrychium, Pteris, Equisetum* and *Selaginella.* Shaded grey bands show intervals with low pollen productivity in MIS 5b, MIS 3 and MIS 2.

TABLES

Table 1. Summary of sedimentary facies and facies associations in VIL sequence.

FACIES	Description
SAND	
Grey Sand	Dm to cm thick calcite and silicate sand.
Creamy sand	Cm to dm-thick layers mostly composed of calcite clasts and charophyte remains. Yellowish, brown or white color depending on variable organic, carbonate and silicate contents.
Peaty Sand	Cm-thick, brown carbonate and silicate sand with peat fragments.
Lumaquella	Mm to cm thick, gastropod-rich sand with calcite matrix.
COARSE SILT	
Yellowish silt	Calcite silt with calcite coating, charophyte remains and calcite crystals and intermediate silicate content.
Creamy silt	Calcite silt, dominated by carbonate coating and calcite crystals and lower silicate content than yellowish silt. Variable reddish mottling.
Light grey silt	Calcite and silicate silt with frequent rootlets and grey mottling.
Dark grey silt	Silicate and calcite silt with organic matter and plant remains. Faintly banded. They are the coarsest silt facies.
Peaty silt	Cm thick layers of coarse grey silt with large peat fragments. Abundant mottling.
FINE SILT	
Light grey silt	Silicate and calcite fine silts. Mottling appears in discrete horizons associated to coarser levels with rootlets and plant fragment.
Creamy/white silt	Layers of finer calcite silt, white, more homogeneous, no gastropods. Creamy layers are more massive to faintly banded (cm-scale) coarser calcite silt, with gastropods, larger calcite clasts, charophyte and organic fragments and higher silicate content.
Black and grey silt	Faintly banded, medium size silt dominated by calcite grains (pseudo-oolites, coatings, calcite clasts) and organic fragments. Grey layers are massive to black, mottled with higher silicate content.
Red clayey silt	Dm thick, massive layers of reddish silt dominated by calcite but abundant silicate content and presence of hematite and dolomite.
Laminated grey/greenish silt	Cm to dm-thick layers of calcite and silicate silt.
PEAT	
Massive fine peat	Cm to dm thick, black, massive, homogeneous fine peat.
Coarse peat	Black, massive with coarse peat fragments.
FACIES ASSOCIATIONS	
A. CARBONATE	Sequences composed of creamy and white sands, coarse and fine yellowish silts and organic silts. Minor peat facies. Varied mottling. **Depositional environment**: littoral charophyte-dominated, carbonate lake. Other intervals with sequences composed of grey sands and grey silts. **Depositional environment**: littoral carbonate lake with higher clastic input.

B. CLASTIC	Sequences dominated by grey sands, coarse grey silts, fine grey silts and massive, black mottled silts. Alternations of dark and light grey coarse silts, with some fine black mottled silts. In more distal areas, sequences are dominated by finer, laminated silts. **Depositional environment**: Clastic dominated, higher energy littoral (current and wave influenced) and lower energy sublittoral to distal.
C. WETLAND	Sequences include peat facies (fine and coarse), peaty sands and silts, lumaquellas and organic-rich silts. Some lastic intercalations and carbonate sands. **Depositional environment**: wetland with some minor carbonate lake.
D. DISTAL ALLUVIAL FAN/MUD FLAT	The sequences are composed of grey, massive to banded silts with frequent mottling and some minor sand layers. Some intervals are dominated by red clayey silts with minor grey silts. **Depositional environment**: distal alluvial fan associated to mudflat.

Table 2. Radiocarbon ages for VIL sequence. Rejected ages are indicated by italics.

Sample	Composite Depth (cm)	Laboratory code	$\delta^{13}C$ (‰)	Radiocarbon age (years BP)	Calibrated age (cal yrs BP) range 2σ
VIL05-1A, 11 cm	11	Beta-332033	27.3	430 ± 30	490 ± 39
VIL05-1A, 132 cm	132	Beta-332034		7460 ± 40	
VIL05-1A, 220 cm	220	Poz-16073		11950 ± 70	
VIL05-1B-1T-2, 2-3 cm	62,5	Beta-319544		2020 ± 30	1974 ± 82
VIL05-1B-1T-2 36-38	96,5	Poz-18451	28,9	3750 ± 40	4084 ± 100
VIL05-1B-1T-3, 6-7	*135*	*Poz-16073*	*32,6*	*11950 ± 70*	*13807 ± 190*
VIL05-1B-1T-3 39-40	173.5	Poz-18509	22,8	7460 ± 50	8279 ± 94
VIL05-1B-1T-4 41-42	233,5	Poz-18453	27,6	9820 ± 50	11248 ± 76
VIL05-1B-1T-5, 55	307,00	Poz-15943		11620 ± 60	13481 ±174
VIL05-1B-1T-6, 15	*325,4*	*Poz-23667*	*32,7*	*5760 ± 60*	*6543 ± 134*
VIL05-1B-1T-7, 25	*370,4*	*Poz-23669*	*25,3*	*6290 ± 40*	*7237 ± 80*
VIL05-1B-1T-7 55-56.5	*417*	*Poz-18510*	*26,4*	*8200 ± 50*	*9157 ± 143*
VIL05-1B-1T-8 32-35	451,5	Poz-18511	22,4	15390 ± 100	18680 ± 193
VIL05-1B-1T-10, 15	549,5	Poz-15944		18280 ± 110	21844 ± 373
VIL05-1B-1T-12 16-17	*638,2*	*Poz-18454*	*25,7*	*22900 ± 280*	*27584 ± 790*
VIL05-1B-1T-14, 5	734,8	Poz-15945		21020 ± 140	25060 ± 503
VIL05-1B-1T-16, 5	861	Poz-15946		22780 ± 160	27447 ± 570
VIL05-1B-1T-18 13-14	*989,5*	*Poz-18455*	*25,4*	*27000 ± 450*	*31501 ± 840*
VIL05-1B-1T-20, 57	1114,8	Poz-23714	5,9	25520 ± 380	30269 ± 713
VIL05-1B-1T-24, 12	1322,1	Poz-15948		27900 ± 300	32182 ± 755
VIL 05 –1B–1T– 28, 7 cm	1487,7	Poz-17394	12,6	33300 ± 800	38285 ± 1892
VIL 05–1B–1T–35, 44 cm	1912,3	Poz-17287	19,4	36800 ± 800	41589 ± 1348
VIL 05–1B–1T–39, 56 cm	*2177,3*	*Poz-17249*	*29,3*	*22920 ± 360*	*27592 ± 928*

Table 3. U/Th samples for VIL sequence (A) and obtained results (B).

A)

Sample ID	Sample weight (g)	Sample name	Composite Depth (m)	Sample type
VIL-1	0.0491	VIL05-1B-1T-61, 40-60	28.9	Carbonate coating
VIL-2	0.0209	VIL05-1B-1T-119, 42-49	45.4	gastropods
		VIL05-1B-1T-121, 33-35	45.7	gastropods
VIL-3	0.0261	VIL05-1B-1T-142, 0-10	52.2	gastropods
	0.0216	VIL05-1B-1T-143, 7-11	52.7	gastropods
	0.0429	VIL05-1B-1T-143, 27-30	52.9	gastropods
VIL-4	0.0852	VIL05-1B-1T-144, 0-5	53.1	gastropods
	0.0261	VIL05-1B-1T-144, 20-22	53.2	gastropods
	0.0216	VIL05-1B-1T-144, 25-33	53.3	gastropods
VIL-5	0.0429	VIL05-1B-1T-118, 40	45.1	Carbonate coating
VIL-6	0.0852	VIL05-1B-1T-112, 10-12	43.4	Carbonate coating

B)

Sample ID	^{238}U Ppb		^{232}Th ppt		δ^{234}U measured^{a}		[^{230}Th/^{238}U] activity^{c}		[^{230}Th/^{232}Th] ppm^{d}		Age uncorrected		Age corrected^{c,e}		δ^{234}U$_{initial}$ corrected^{b}	
VIL-1	564	± 1.5	456003	± 7657	957.8	± 4.6	3.91658	± 0.092	79.8	± 2.3	-	-	-	-	-	-
VIL-2	167	± 0.6	90183	± 567	78.8	± 6.4	1.04223	± 0.028	31.8	± 0.9	313 784.7	± 51327.8	299 669.8	± 45407.0	183.8	± 33.3
VIL-3	100	± 0.4	2738	± 29	148.0	± 8.0	1.02330	± 0.014	614.3	± 10.5	216 876.0	± 10444.8	216 246.9	± 10389.0	272.7	± 16.9
VIL-4	111	± 0.5	2276	± 34	104.0	± 8.8	1.04494	± 0.013	840.5	± 16.2	276 135.6	± 19331.9	275 648.7	± 19246.1	226.6	± 23.4
VIL-5	337	± 0.7	464119	± 8122	18.0	± 2.6	1.48947	± 0.102	17.8	± 1.3	-	-	-	-	-	-
VIL-6	190	± 0.4	41233	± 188	2.4	± 2.4	1.16244	± 0.011	88.1	± 0.9	-	-	-	-	-	-

Analytical errors are 2σ of the mean. [a] $\delta^{234}U = ([^{234}U/^{238}U]_{activity} - 1) \times 1000$; [b] $\delta^{234}U_{initial}$ corrected was calculated based on ^{230}Th age (T), i.e., $\delta^{234}U_{initial} = \delta^{234}U_{measured}\ X\ e^{\lambda 234*T}$, and T is corrected age. [c] $[^{230}Th/^{238}U]_{activity} = 1 - e^{-\lambda 230T} + (\delta^{234}U_{measured}/1000)[\lambda_{230}/(\lambda_{230} - \lambda_{234})](1 - e^{-(\lambda 230 - \lambda 234)\,T})$, where T is the age. Decay constants are 9.1577×10^{-6} yr^{-1} for ^{230}Th, 2.8263×10^{-6} yr^{-1} for ^{234}U, and 1.55125×10^{-10} yr^{-1} for ^{238}U (Cheng et al., 2000). [d] The degree of detrital ^{230}Th contamination is indicated by the [^{230}Th/^{232}Th] atomic ratio instead of the activity ratio. [e] Age corrections were calculated using an average crustal ^{230}Th/^{232}Th atomic ratio of $4.4 \times 10^{-6} \pm 2.2 \times 10^{-6}$. Those are the values for a material at secular equilibrium, with the crustal ^{232}Th/^{238}U value of 3.8. The errors are arbitrarily assumed to be 50%.

Table 4. Dose rate data, multi-grain aliquot additive dose equivalent doses (D_e) and polymineral fine-grain IRSL ages for VIL samples.

Sample	Sample depth (m)	Grain size (µm)	water content [a]	*α*-value [b]	Total dose rate [c, d]	D_e (Gy) [d]	OSL age (ka) [d]
MAD-5172SDA	18.0	2-10	26	0.08	0.83 ± 0.06	34 ± 1	40.4 ± 3.5
MAD-5173SDA	47.0	2-10	26	0.11	1.05 ± 0.07	76 ± 2	72.5 ± 5.1
MAD-5196SDA	54.0	2-10	20	0.16	1.27 ± 0.08	119 ± 4	93.6 ± 6.8
MAD-5200SDA	71.0	2-10	30	0.22	2.84 ± 0.22	329 ± 3	115.9 ± 9.0
MAD-5203SDA	73.0	2-10	30	0.08	0.94 ± 0.04	114 ± 6	120.8 ± 8.2

[a] Field water content, expressed as % of dry mass of mineral fraction, with an assigned relative uncertainty of ±1%.
[b] Alpha effectiveness value used for alpha dose rate calculation, determined using the approach of Zimmerman (1972).
[c] Total dose rate comprises alpha, beta, gamma and cosmic-ray contributions. Beta and gamma dose rates were determined from ^{40}K, ^{238}U and ^{232}Th activities calculated on dried and homogenised, bulk sediment samples using a combination of beta counting and thick source alpha counting. The conversion factors of Nambi and Aitken (1986) were used to derive dose rate estimates from measured activities.
[d] Mean ± total uncertainty (68% confidence interval), calculated as the quadratic sum of the random and systematic uncertainties.

Table 5. Dose rate data, single-grain equivalent doses (D_e) and quartz OSL ages for VIL samples

Sample	Sample depth (m)	Grain size (µm)	Measured water content [a]	Compaction-corrected water content [b]	Environmental dose rate (Gy/ka)				Equivalent dose (D_e) data				OSL age (ka) [e, j]
					Beta dose rate [c]	Gamma dose rate [c]	Cosmic dose rate [d]	Total dose rate [e, f]	No. of grains [g]	Overdis-persion (%) [h]	Age model [i]	D_e (Gy) [e]	
V49	27.0	180 – 250	27 ± 7	30 ± 8	1.60 ± 0.08	0.95 ± 0.03	0.05 ± 0.01	2.64 ± 0.21	72 / 1100	29 ± 4	MAM-4	129 ± 18	49.0 ± 7.9
V58	31.6	212 – 250	13 ± 3	15 ± 4	0.91 ± 0.05	0.63 ± 0.03	0.04 ± 0.01	1.62 ± 0.10	93 / 1000	37 ± 4	MAM-4	116 ± 13	71.6 ± 9.4
V67	36.6	212 – 250	19 ± 5	21 ± 5	1.53 ± 0.08	1.01 ± 0.03	0.04 ± 0.01	2.61 ± 0.17	60 / 1000	18 ± 6	CAM	191 ± 9	73.2 ± 6.1
V99	51.8	212 – 250	12 ± 3	14 ± 4	0.85 ± 0.04	0.60 ± 0.02	0.02 ± 0.01	1.51 ± 0.08	75 / 1000	29 ± 4	MAM-4	128 ± 16	84.6 ± 11.3
V110	56.8	180 – 250	27 ± 7	35 ± 9	0.91 ± 0.05	0.64 ± 0.03	0.02 ± 0.01	1.60 ± 0.14	71 / 900	29 ± 4	MAM-4	167 ± 16	104.5 ± 14.1
V117	59.8	212 – 250	24 ± 6	28 ± 7	0.81 ± 0.05	0.57 ± 0.02	0.02 ± 0.01	1.43 ± 0.11	94 / 1200	26 ± 3	MAM-4	180 ± 18	126.3 ± 16.2
V127	63.9	212 – 250	13 ± 3	16 ± 4	1.23 ± 0.06	0.77 ± 0.03	0.02 ± 0.01	2.06 ± 0.12	81 / 1300	13 ± 3	CAM	264 ± 9	128.1 ± 9.1
V135	67.5	212 – 250	23 ± 6	28 ± 7	0.95 ± 0.05	0.64 ± 0.03	0.02 ± 0.01	1.64 ± 0.14	63 / 1000	22 ± 4	CAM	220 ± 10	134.1 ± 12.8
V148	72.7	212 – 250	14 ± 3	19 ± 5	1.02 ± 0.05	0.66 ± 0.02	0.02 ± 0.01	1.72 ± 0.11	75 / 1000	22 ± 4	CAM	236 ± 11	137.0 ± 10.9

[a] Field water content, expressed as % of dry mass of mineral fraction, with an assigned relative uncertainty of ±25%.

[b] Corrected field water contents used to calculate the final OSL ages for these samples. Full details of the procedures used to derive these compaction-correction water contents are provided in the Supplementary Information. This correction has been included because of the relatively thick sediment overburdens affecting these samples and, hence, the increased likelihood of sediment compaction and dewatering effects with time.

[c] Measurements made on dried and powdered samples by high-resolution gamma-ray spectrometry. Specific activities have been converted to dose rates using the conversion factors given in Guérin *et al.* (2011), making allowance for beta-dose attenuation (Mejdahl, 1979; Brennan, 2003).

[d] Cosmic-ray dose rates were calculated using the approach of Prescott and Hutton (1994) and assigned a relative uncertainty of ±10%.

[e] Mean ± total uncertainty (68% confidence interval), calculated as the quadratic sum of the random and systematic uncertainties.

[f] Includes an internal dose rate of 0.03 Gy/ka with an assigned relative uncertainty of ±30%.

[g] Number of D_e measurements that passed the SAR rejection criteria and were used for D_e determination / total number of grains analysed.

[h] The relative spread in the D_e dataset beyond that associated with the measurement uncertainties for individual D_e values, calculated using the central age model (CAM) of Galbraith *et al.* (1999).

[i] Age model used to calculate the sample-averaged D_e value for each sample. MAM-4 = 4-parameter minimum age model of Galbraith *et al.* (1999). The MAM-4 has been preferred over the 3-parameter minimum age model (MAM-3) for these single-grain datasets on statistical grounds using the maximum log likelihood (L_{max}) score criterion outlined by Arnold et al. (2009). MAM-4 D_e estimates were calculated after adding, in quadrature, a relative error of 10% to each individual D_e measurement error to approximate the minimum underlying dose overdispersion observed in the single-grain dose-recovery test and in an 'ideal' (well-bleached and unmixed) sedimentary sample from this core (sample V127).

[j] Total uncertainty includes a systematic component of ±2% associated with laboratory beta-source calibration.

Table 6. High-resolution gamma spectrometry results and daughter-to-parent isotopic ratios for VIL single-grain OSL samples.

Sample	Sample depth (m)	Radionuclide specific activities (Bq/kg) [a, b]						Daughter/ parent isotopic ratio		
		^{238}U	^{226}Ra	^{210}Pb	^{228}Ra	^{228}Th	^{40}K	^{226}Ra/^{238}U	^{210}Pb/^{226}Ra	^{228}Th/^{228}Ra
V49	27.0	22.5 ± 4.4	25.5 ± 1.9	26.1 ± 2.2	38.5 ± 3.3	39.0 ± 2.8	763 ± 26	1.13 ± 0.24	1.02 ± 0.12	1.01 ± 0.11
V58	31.6	28.9 ± 4.8	25.0 ± 1.7	25.2 ± 3.2	23.8 ± 2.9	24.2 ± 1.4	303 ± 11	0.86 ± 0.16	1.01 ± 0.15	1.02 ± 0.14
V67	36.6	27.5 ± 4.8	22.8 ± 2.3	25.0 ± 3.2	46.8 ± 5.6	46.6 ± 5.3	624 ± 21	0.83 ± 0.17	1.09 ± 0.18	1.00 ± 0.16
V99	51.8	16.4 ± 2.7	18.0 ± 1.3	18.2 ± 2.1	25.5 ± 3.1	26.1 ± 3.4	302 ± 11	1.10 ± 0.19	1.01 ± 0.14	1.02 ± 0.18
V110	56.8	31.4 ± 4.3	32.6 ± 2.3	34.8 ± 4.2	26.5 ± 3.2	26.8 ± 2.9	367 ± 13	1.04 ± 0.16	1.07 ± 0.15	1.01 ± 0.16
V117	59.8	23.1 ± 4.8	23.7 ± 2.5	23.8 ± 2.8	25.4 ± 3.1	25.0 ± 5.4	317 ± 11	1.03 ± 0.24	1.00 ± 0.16	0.99 ± 0.24
V127	63.9	24.4 ± 4.1	22.9 ± 1.7	22.0 ± 2.8	29.2 ± 3.5	30.2 ± 2.1	477 ± 16	0.95 ± 0.17	0.96 ± 0.14	1.03 ± 0.14
V135	67.5	29.1 ± 4.9	28.9 ± 2.1	27.5 ± 3.4	29.0 ± 3.5	23.6 ± 4.1	380 ± 13	0.99 ± 0.18	0.95 ± 0.14	0.81 ± 0.17
V148	72.7	20.2 ± 2.7	21.3 ± 1.5	22.0 ± 2.7	25.3 ± 3.0	24.9 ± 2.1	397 ± 13	1.06 ± 0.16	1.03 ± 0.14	0.98 ± 0.14

[a] Measurements made on dried and powdered samples by high-resolution gamma-ray spectrometry.
[b] Mean ± total uncertainty (68% confidence interval), calculated as the quadratic sum of the random and systematic uncertainties.

Supplementary material

OSL DATING METHOD

Multi-grain aliquot infrared stimulated luminescence (IRSL)

Polymineral fine-grain equivalent dose (De) estimates were determined from ultraviolet emissions using a multiple aliquot additive dose (MAAD) protocol and a preheat of 180 ºC for 10 s prior to IRSL stimulation. Environmental dose rates were calculated on dried and homogenised, bulk sediment samples using a combination of beta counting and thick source alpha counting. Cosmic-ray dose rate contributions were calculated from high energy gamma emissions recorded in situ using a NaI(Tl) gamma spectrometer. For alpha dose rate calculations, alpha effectiveness (a-values) were determined on a sample-by-sample basis by comparing IRSL signals induced by 3.7 MeV alpha particles (using a 241Am source) with corresponding signals induced by beta irradiation (using the 90Sr/90Y source) (Zimmerman, 1972). The conversion factors of Nambi and Aitken (1986) were used to derive dose rate estimates from measured elemental concentrations and specific activities. The final dose rates have also been adjusted for water attenuation effects (Aitken, 1985), using present-day sediment moisture contents.

Environmental dose rate calculations for the single-grain OSL samples

Environmental dose rates were calculated for the single-grain OSL samples using high-resolution gamma spectrometry measurements made with high-purity Ge detectors (an n-type closed-end coaxial system and a p-type well system). Specific activities were obtained for ^{238}U (determined from ^{235}U emissions after correcting for ^{226}Ra interference), ^{226}Ra (derived from ^{214}Pb and ^{214}Bi emissions), ^{210}Pb, ^{228}Ra (derived from ^{228}Ac emissions), ^{228}Th (derived from ^{212}Pb, ^{212}Bi and ^{208}Tl emissions) and ^{40}K from dried and homogenised, bulk sediment sub-samples. Beta and gamma dose rates were calculated from these specific activities using the conversion factors given in Guérin et al. (2011), making allowance for beta-dose attenuation (Mejdahl, 1979; Brennan, 2003). Account was also taken of the cosmic-ray dose rate contribution, adjusted for site altitude, geomagnetic latitude and thickness of sediment overburden (Prescott and Hutton, 1994), and assuming a steady rate of overburden accumulation from the time of sample deposition to the present day. The beta, gamma and cosmic-ray dose rates have been corrected for estimated long-term sediment water contents (Aitken, 1985). We have also included an assumed effective internal alpha dose rate of 0.03 ± 0.01 Gyka-1 in the final dose rate calculations, based on published internal ^{238}U and ^{232}Th measurements for etched quartz grains from a range of locations (e.g. Mejdahl, 1987; Bowler et al. 2003) and an alpha efficiency factor (a-value) of 0.04 ± 0.01 (Rees-Jones, 1995).

Compaction-corrected water content analysis for the single-grain OSL samples

The as measured water contents determined from the sampled sections of the cores vary between 13 and 27% but lack a systematic decrease down the core profile. These characteristics reflect the heterogeneous nature of the sedimentary facies within Units IV-VII and preclude a site-specific empirical correction of sediment overburden thickness versus water content (e.g. Olley et al., 2004b; Lukas et al., 2012). In light of these complications, we have approximated progressive changes in water content with time by assuming a uniform deposition rate and an exponential compaction relationship between sediment porosity and depth, following the widely-used equation of Athy (1930) and Sclater and Christie (1980), Eq.1, where θ(z) is fractional porosity at burial depth z (km), θ0 is surface porosity at z = 0 km, and k (km-1) is an empirically derived compaction coefficient expressing the rate at which porosity decreases with depth. In this study we have used a k value of 1.16 km-1 following the empirical porosity / depth relationship established by Gallagher and Lambeck (1989) for non-marine, silt-sized sedimentary deposits.

The porosity of each sample (equivalent to θ(z) at the current burial depth) was calculated from laboratory measurements of gravimetric saturated water content, dry sediment volume and bulk density, and an assumed grain density of 2.65 gcm-3, according to Eq. 1-6 of Lukas et al. (2012). The expected surface porosity for each sample was then back-calculated using Eq. 1. After establishing a fixed representative θ0 value for each sample, Eq. 1 was subsequently rearranged and used to iteratively solve θ(z) at 1 m intervals for all depths between 0 km and the present-day sample depth. The long-term (compaction-corrected) porosity value for the burial period of each sample was taken as the average of the integrated θ(z) values over the exponential porosity-depth profile between the surface and final sample burial depth, following Kadereit et al. (2012). Corresponding compaction-corrected gravimetric water contents were calculated from the long-term (compaction-corrected) porosity values using Eq. 1-6 of Lukas et al. (2012).

The compaction-corrected water contents shown in Table 5 do not take into account potential variations in moisture that may have been caused by changing lake and groundwater conditions during past glacial-interglacial cycles. Such sources of variability are difficult, if not impossible, to constrain accurately on an individual sample basis.

We have therefore pragmatically accounted for temporal variability in our long-term moisture assessments by assigning a large relative uncertainty of ±25% to each compaction-corrected water content estimate. Though the modelled water contents obtained using the aforementioned approach are based on approximate estimates of sediment compaction, it is worth emphasising that the final dose rate calculations are relatively insensitive to our choice of compaction correction. Specifically, the modelled water contents are only 2-8% higher in absolute terms, and 14-34% higher in relative terms, in comparison to the original 'as measured' water contents. Similarly, the resultant dose rates obtained using the modelled and as measured water contents differ by <0.16 Gyka-1 and the corresponding final ages obtained using the two alternative methods of long-term moisture assessment are consistent with each other at 1σ for all samples.

References

Athy, L.F. 1930. Density, porosity and compaction of sedimentary rocks. Bulletin of the American Association of Petroleum Geologists 14,1-24.

Gallagher, K., Lambeck, K. 1989. Subsidence, sedimentation and sea-level changes in the Eromanga Basin, Australia. Basin research 2, 115-131.

Kadereit, A., DeWitt, R., Johnson, T.C., 2012. Luminescence properties and optically (post-IR blue-light) stimulated luminescence dating of limnic sediments from northern Lake Malawi – Chances and limitations. Quaternary Geochronology 10, 160-166.

Lukas, S., Preusser, F., Anselmetti, F.S., Tinner, W., 2012. Testing the potential of luminescence dating of high-alpine lake sediments. Quaternary Geochronology 8, 23-32.

Olley, J.M., De Deckker, P., Roberts, R.G., Fifieldd, L.K., Yoshida, H., Hancock, G., 2004b. Optical dating of deep-sea sediments using single grains of quartz: a comparison with radiocarbon. Sedimentary Geology 169, 175-189.

BACON AGE-DEPTH MODEL

1. Assessing the influence of priors on the predictive accuracy of Bacon models: the role of acc.mean y acc.shape

The accumulation rate prior is a gamma distribution defined by two parameters: mean (named acc.mean in Bacon, and provided by the user in yr/cm), and shape (acc.shape). The chosen values in the sensitivity analysis for the accumulation mean were 10, 15, 20, 25 and 30, and the values defining the shape of the distribution were 1, 2, 3, 4 and 5.

The memory prior is a beta distribution with values between 0 and 1 describing the temporal autocorrelation of the accumulation rate. Lower values indicate highly variable sedimentation conditions, while higher values indicate more constant accumulation rates. The parameters describing this distribution are memory mean (mem.mean), and memory strength (mem.strength). The values for the memory mean parameter were 0.1, 0.3, 0.5, 0.7 and 0.9, while the memory strength values were 1, 5, 10, 15 and 20. Due to the high number of Bacon models to calibrate (7500), for computational limitations we established the thick parameter to 50. This is not the optimum value to calibrate a definitive age-depth model, but it offers a good trade-off between fit and computation speed, since it was beyond our capabilities to test all the possible combinations of Bacon parameters.

To evaluate the effect of the different combinations of parameter values used to define the priors over the model predictive accuracy, we used a “leave-one-date-out” cross-validation approach (Parnell et al. 2011). This procedure implies that for every possible combination of parameters we calibrate as many models as dates are available in the input dataset (except the earliest and the oldest date, that were used as anchor points). Each model was calibrated removing one of the dates and thus the absolute difference between the calibrated (true age) and the modelled age was computed, and interpreted as a proxy of the predictive error. On each iteration we stored the following data in the results table: parameter values (mem.strength ,mem.mean, acc.mean and acc.shape), identifier of the excluded date, depth of the excluded date, calibrated and predicted age of the excluded date, predictive error, and depth interval between the contiguous dates to the one excluded. This procedure was performed separately for C14 and OSL. OSL dates have confidence intervals that are at least an order of magnitude wider than the ones of C14 dates. Therefore the removal of a single OSL date during the leave-one-out cross validation has the potential to artificially increase the overall error measured in C14 dates, making the results difficult to interpret.

We analysed the results graphically, by plotting the average error and the error of each date against the parameter values, and used Linear Mixed Effects Models (R package 'nlme', Pinheiro et al. 2014) selecting the identifier of the dates as a random effect. We evaluated the magnitude of the effect of the different parameters on the error, and explore potential interactions among parameters. The knowledge obtained during this sensitivity analysis was finally used to calibrate a final age-depth model for VIL, by selecting parameters maximizing the overall predictive accuracy of the model while maintaining enough flexibility to represent properly the changes in accumulation rate and memory of this large core.

The average predictive error of the Bacon age-depth models remained constant through the range of values selected for the different parameter values, both for 14C and OSL dates. When analysing the results date by date, the GLMM showed that changes in the values of the memory mean and strength do not affected significantly the predictive error (Table 1).

But when analysing the results of the accumulation rate prior, we found a complex pattern. For the radiocarbon dates we found a significant negative covariation (see Table 1 and Fig. 1) between the values of the mean accumulation rate and the the predictive error, but only in the three deepest dates (1141.3, 1317.9 and 1493.5 cm). The OSL dates between 3160 and 5357.4 cm showed the same pattern (Fig. 2).

Table 1: Results of the Generalized Linear Mixed Models

Dating method	Parameter	Estimate	Deviation	T-value	P-value
RC	Acc.mean	10.4423	0.4188	24.93458	**0.0000**
OSL	Acc.mean	-40.883	11.2345	-3.639057	**0.0003**
RC	Acc.shape	12.583	2.1743	5.787179	**0.0000**
OSL	Acc.shape	408.076	56.0203	7.284427	**0.0000**
RC	Interaction acc.mean-acc.shape	4.9132	0.2899	16.945519	**0.0000**
OSL	Interaction acc.mean-	42.534	7.8996	5.384274	**0.0000**

	acc.shape				
RC	Mem.mean	8.9227	10.8952	0.818952	0.4128
OSL	Mem.mean	0.114	280.440	0.000405	0.9997
RC	Mem.strength	-0.0727	0.4536	-0.160343	0.8726
OSL	Mem.strength	0.313	11.6135	0.026921	0.9785

From 5680 to 7270 cm the pattern changed drastically, with predictive error decreasing with increasing values of the mean accumulation rate. Three OSL dates (2700, 5680 and 7200 cm) showed a minimum in the predictive error when the mean of the accumulation rate reached 20 yr/cm. The acc.shape parameter showed a similar and statistically significant pattern (see Table 1), with a decreased error with lower acc.shape values for the deepest 14C dates (Fig. 3), and all OSL dates except those at 5980, 6390 and 6750 cm (Fig. 4). As expected, there was a significant interaction between the parameters acc.mean and acc.shape, with decreasing values of both parameters leading to lower predictive errors in the calibrated Bacon models.

In order to perform a single model with all radiocarbon and OSL dates we set up a compromise between the best acc.mean for radiocarbon and OSL, especially for the older ages of the latter. Thus we set acc.mean in 30 yr/cm, while acc.shape was set at 1 as it reduces the error for the whole set of dates.

Figure 1: Effect of different values for the accumulation mean parameter for the radiocarbon dated samples.

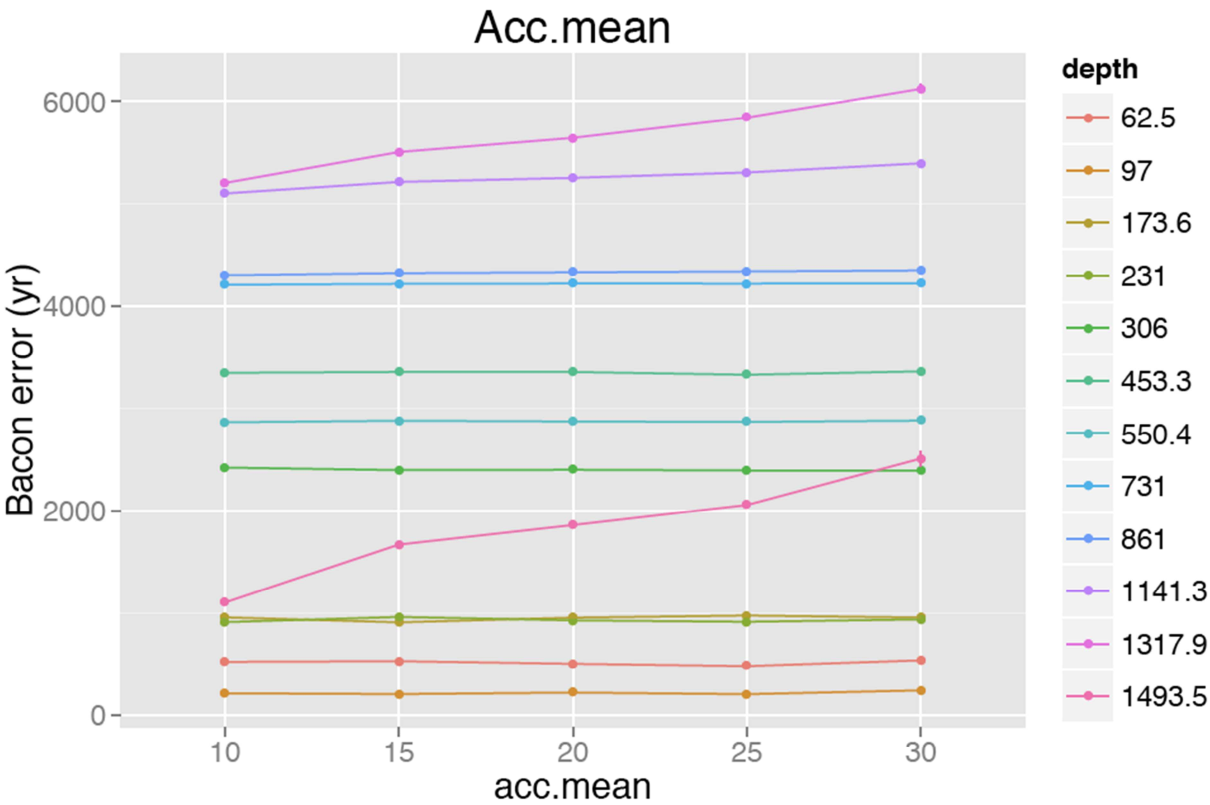

Figure 2: Effect of different values for the accumulation mean parameter for the IRSL and OSL dated samples.

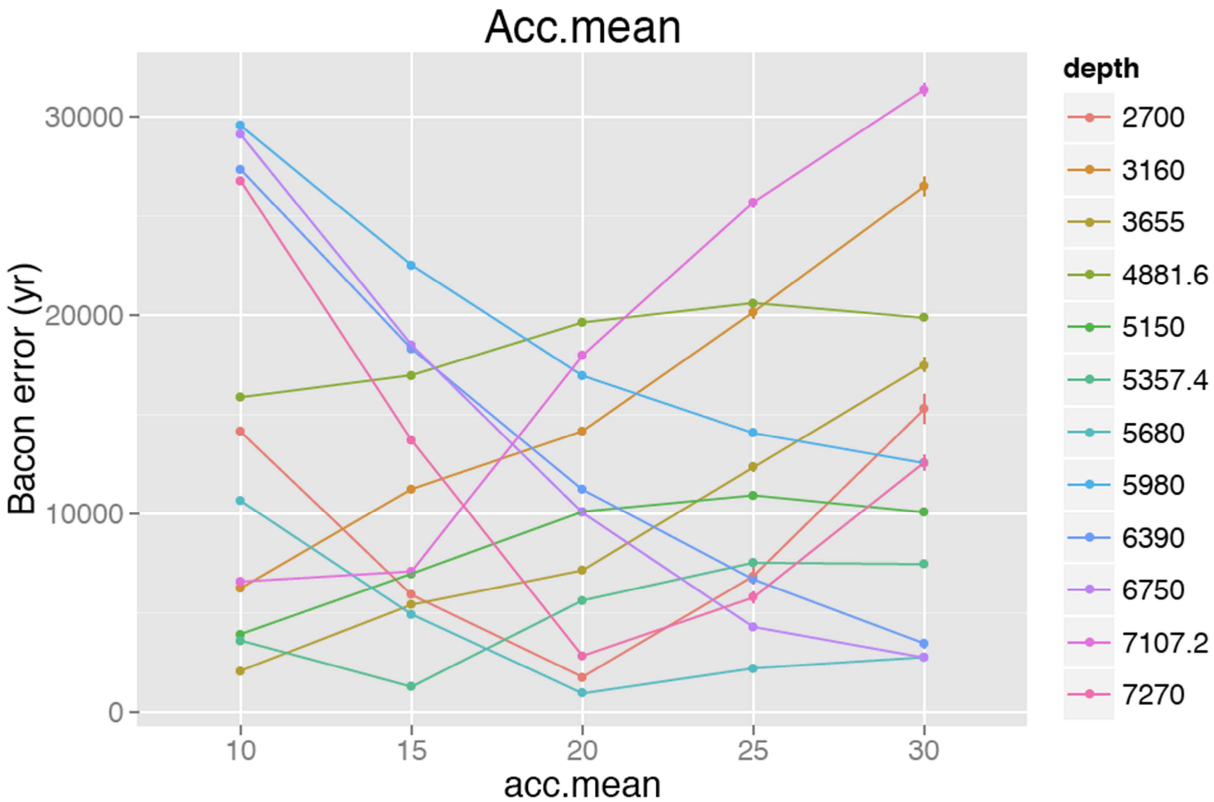

Figure 3: Effect of different values for the accumulation shape parameter for the radiocarbon dated samples.

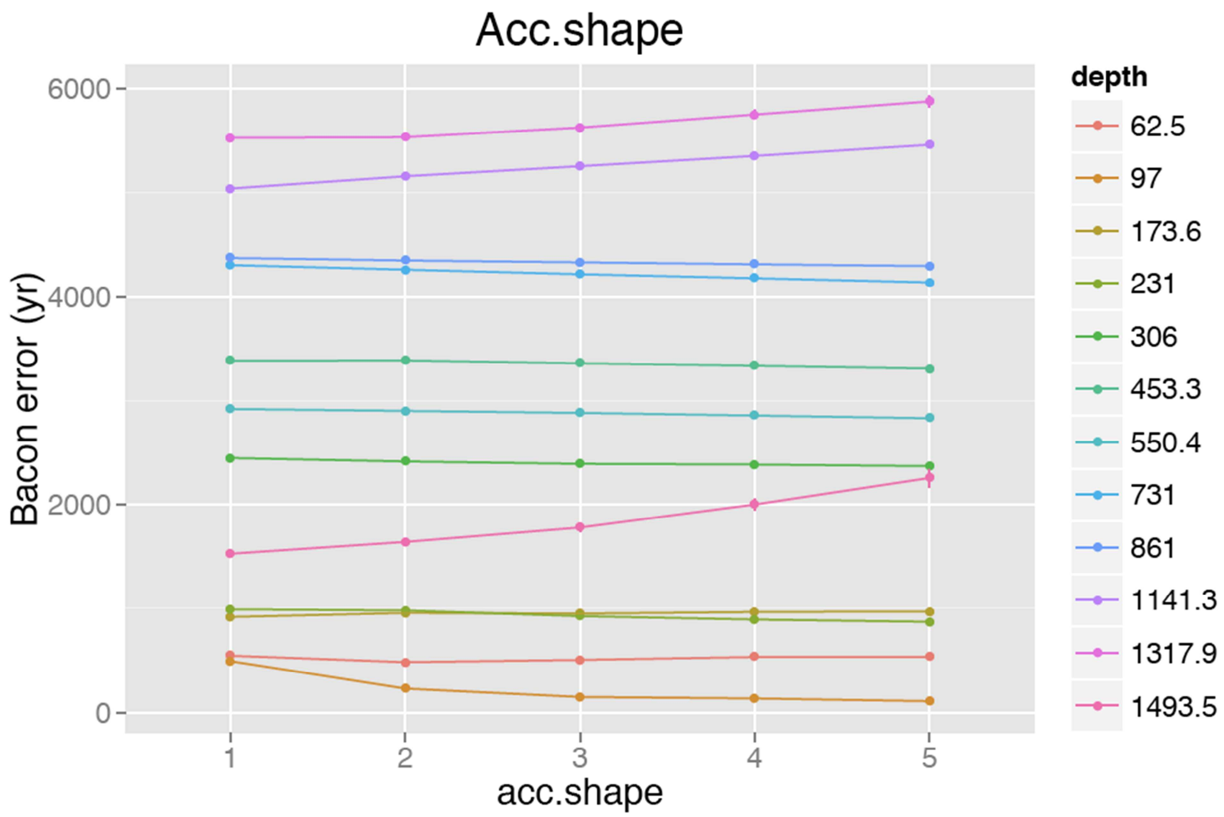

Figure 4: Effect of different values for the accumulation shape parameter for the IRSL and OSL dated samples.

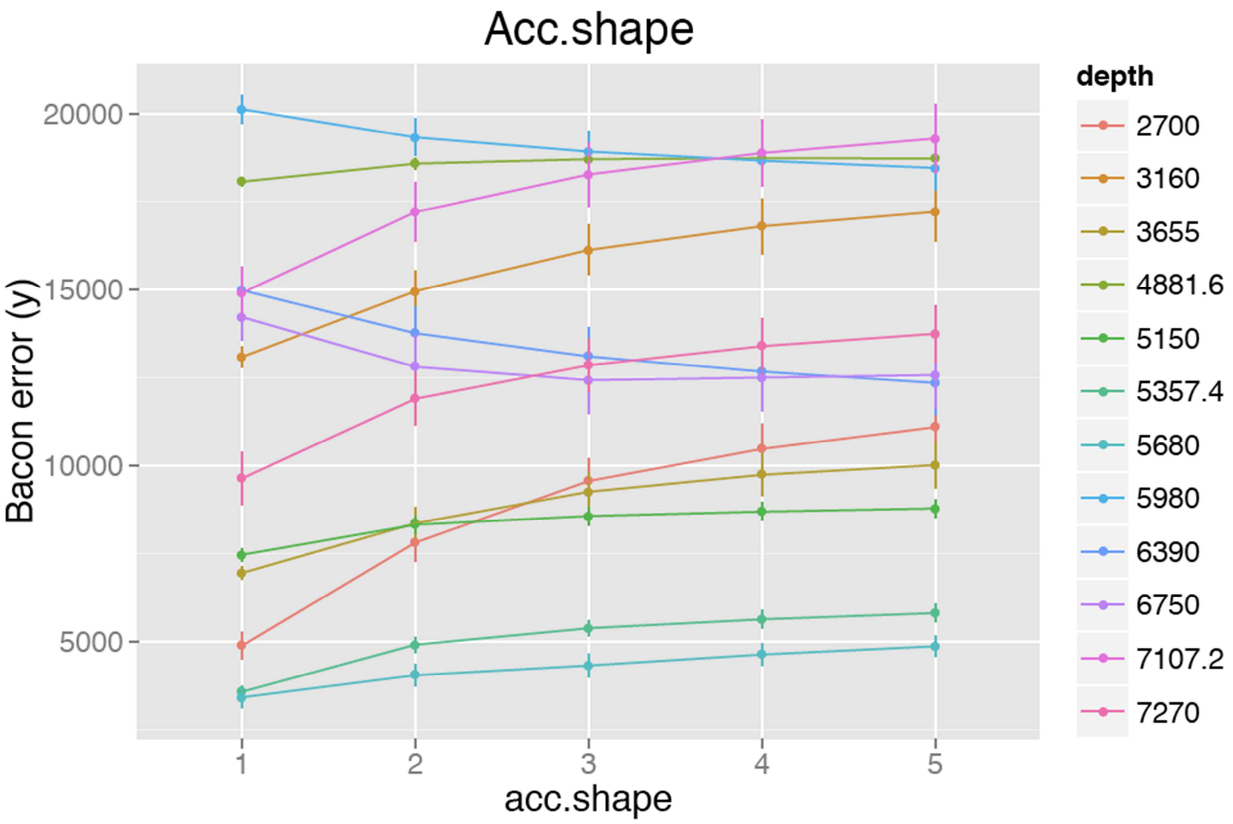

2. Final Bacon age-depth model: code and data used

Villarquemado final depth-age model included 30 dated samples (Table 2) that were modelled using a modified version of Bacon v2.2 (http://chrono.qub.ac.uk/blaauw/manualBacon_2.3.pdf). The code and data used have been upload to the data repository Mendeley Data

Lab ID	Dating Technique	Depth (cm)	Age	Error
Beta-332033	radiocarbon	11	430	30
Beta-319544	radiocarbon	62.5	2020	30
Poz-18451	radiocarbon	97	3750	40
Beta-332034	radiocarbon	132	7460	40
Poz-18509	radiocarbon	173.6	7460	50
Poz-16073	radiocarbon	220	11950	70
Poz-18453	radiocarbon	231	9820	50
Poz-15943	radiocarbon	306	11620	60
Poz-18511	radiocarbon	453.3	15390	100
Poz-15944	radiocarbon	550.4	18280	110
Poz-15945	radiocarbon	731	21020	140
Poz-15946	radiocarbon	861	22780	160
Poz-23714	radiocarbon	1141.3	25520	380
Poz-15948	radiocarbon	1317.9	27900	300
Poz-17394	radiocarbon	1493.5	33300	800
MAD-5172SDA	IRSL	1832.1	40421	3468
Poz-17287	radiocarbon	1915.4	36800	800
V-49	OSL	2700	49000	8000
V-58	OSL	3160	71700	9500
V-67	OSL	3655	73300	6400
MAD-5173SDA	IRSL	4881.6	72457	5152
V-99	OSL	5150	84700	11500
MAD-5196SDA	IRSL	5357.4	93551	6816
V-110	OSL	5680	104500	14100
V-117	OSL	5980	126500	16500
V-127	OSL	6390	128000	9500
V-135	OSL	6750	134200	13200
MAD-5200SDA	IRSL	7107.2	115890	8996
V-148	OSL	7270	137100	11400
MAD-5203SDA	IRSL	7329.5	120808	8209

Table 2: Data set used for building the final Villarquemado depth-age model.

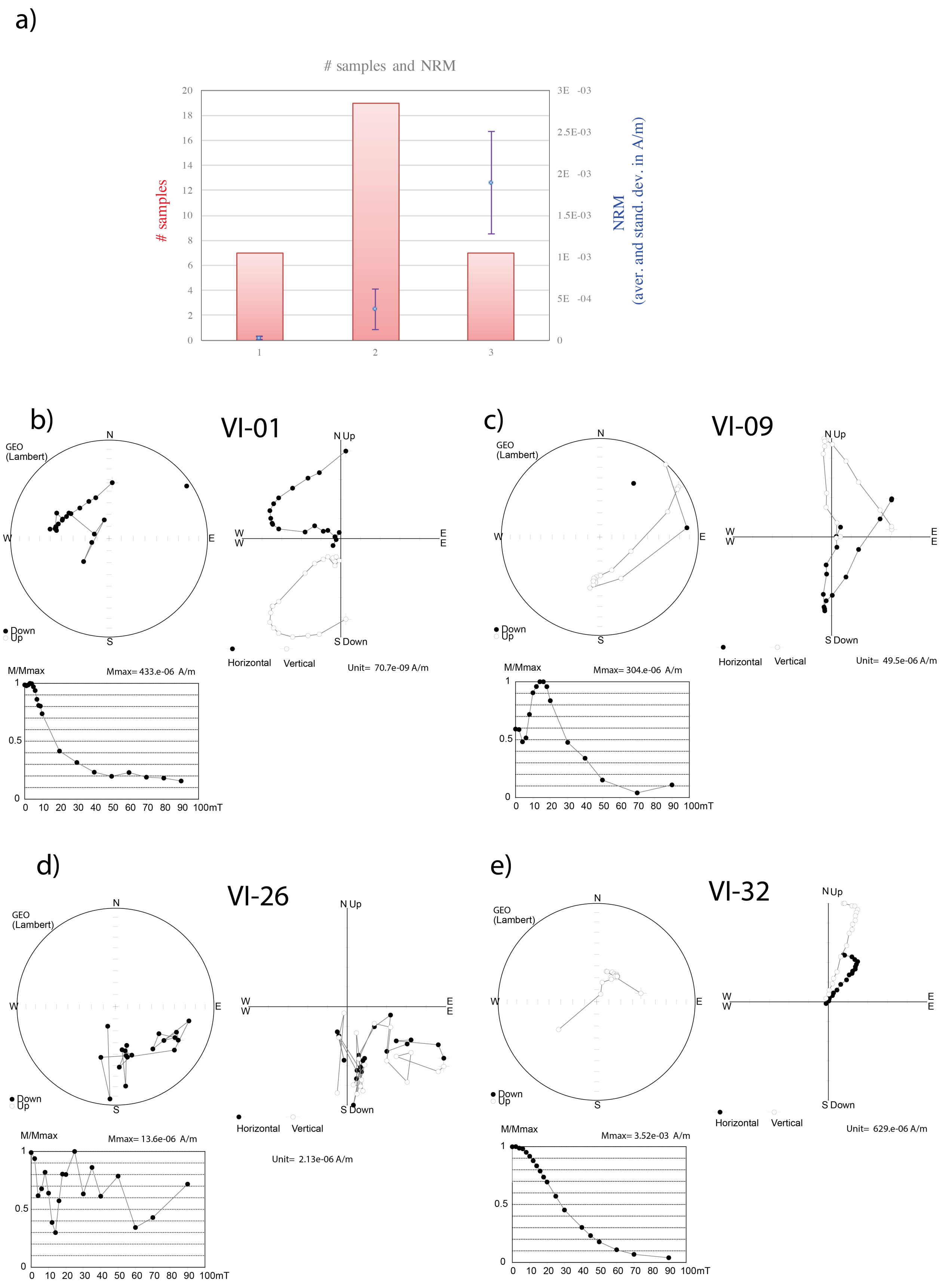

a)
samples and NRM
samples
NRM
(aver. and stand. dev. in A/m)
b)
VI-01
c)
VI-09
d)
VI-26
e)
VI-32
GEO
(Lambert)
Down
Up
N Up
S Down
Horizontal
Vertical
Unit= 70.7e-09 A/m
Unit= 49.5e-06 A/m
Unit= 2.13e-06 A/m
Unit= 629.e-06 A/m
M/Mmax
Mmax= 433.e-06 A/m
Mmax= 304.e-06 A/m
Mmax= 13.6e-06 A/m
Mmax= 3.52e-03 A/m
100mT

f)

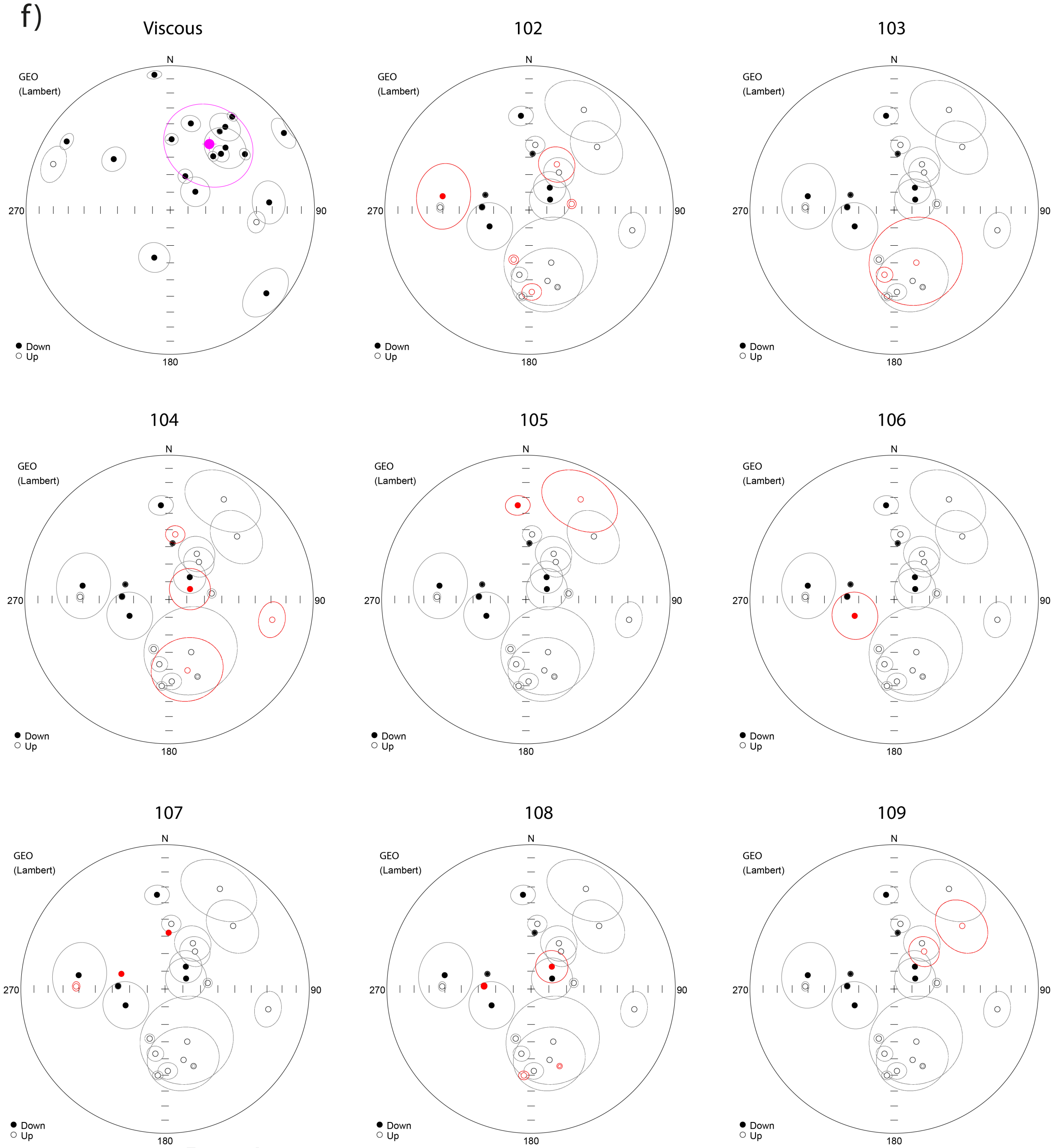
Viscous
102
103
104
105
106
107
108
109
N
GEO
(Lambert)
270
90
180
Down
Up

(a) V127: 300 Gy dose-recovery test

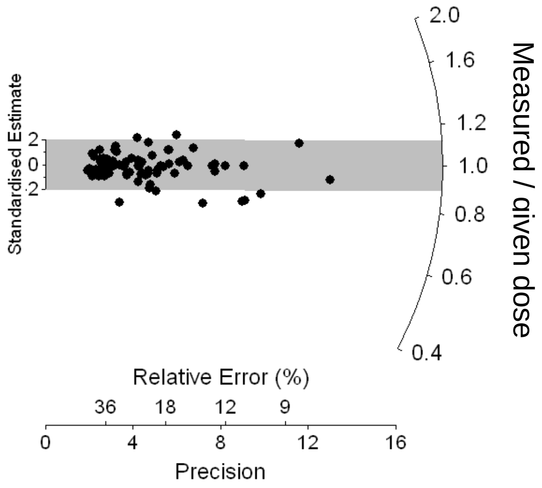

(b) V127: Natural D_e values

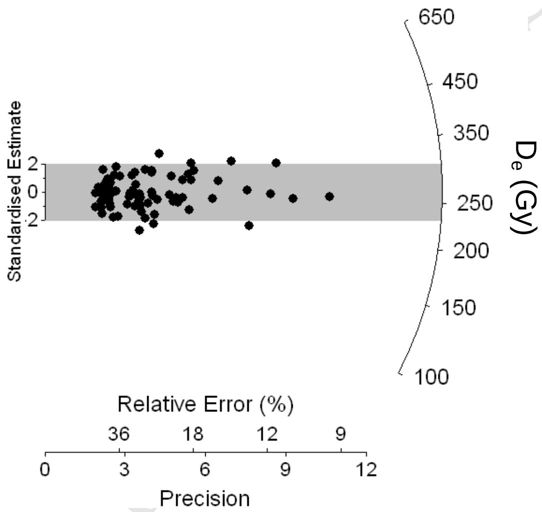

(c) V99: Natural D_e values

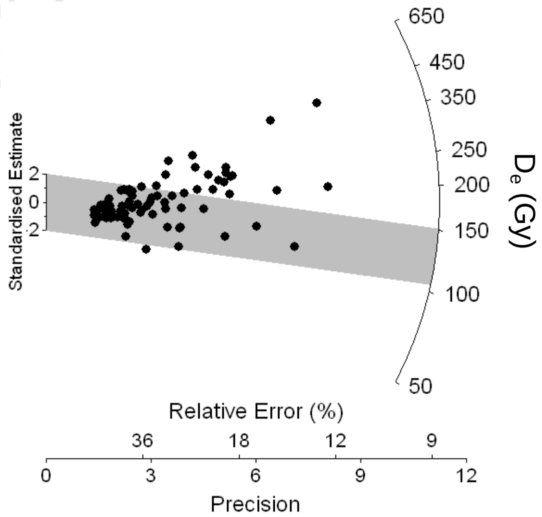

Figure 1. A. Location of Cañizar de Villarquemado Basin. B. Map of the watershed and maximum surface area of the wetland prior to drainage.

A

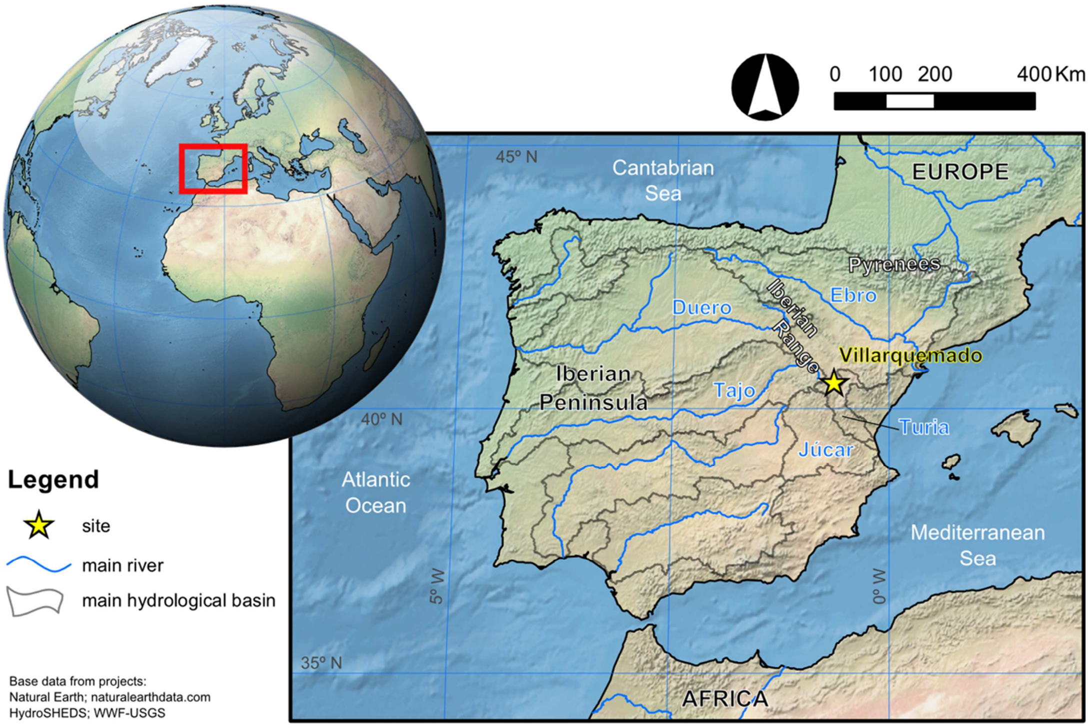

B

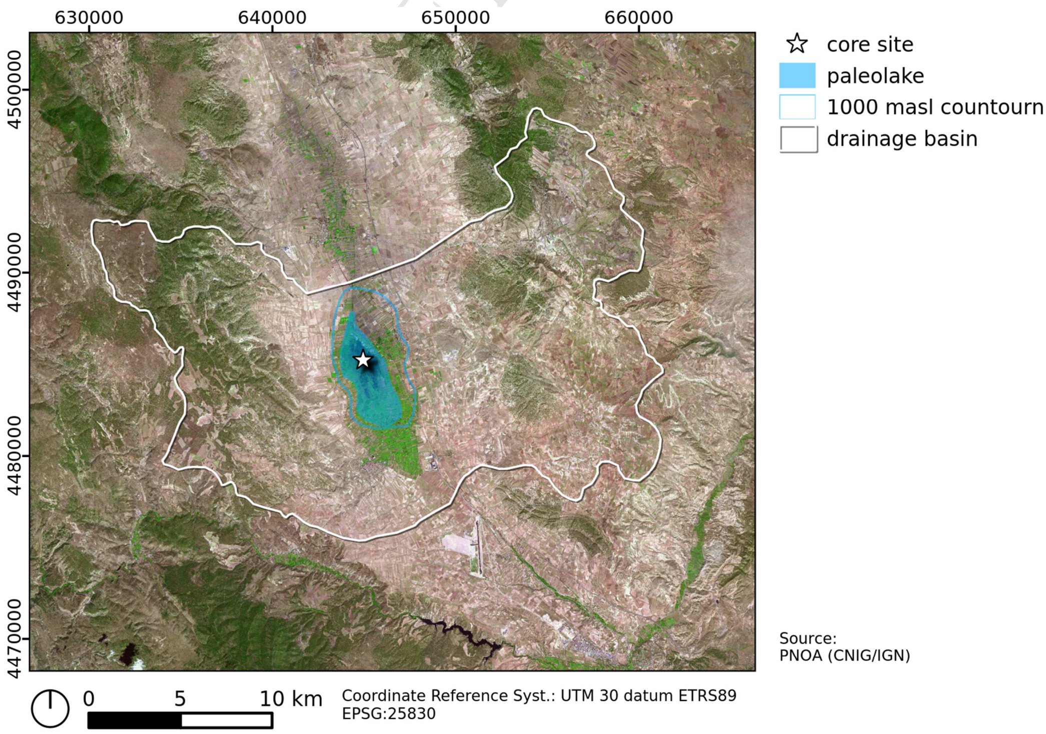

Figure 2. Stratigraphy of the VIL sequence: sedimentary facies and associations, units, depositional environments and location of samples for different dating methods.

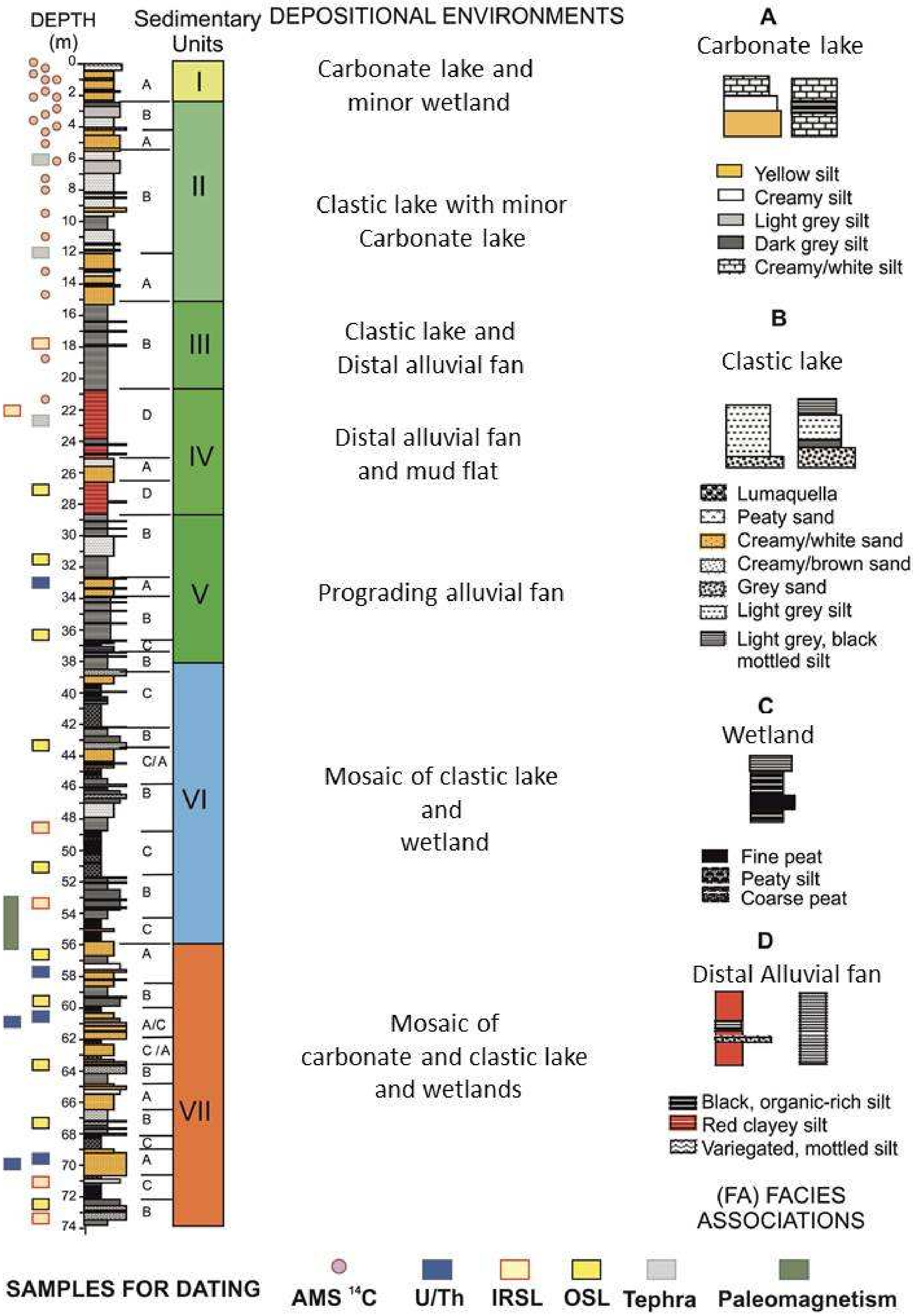

Figure 5. The Bayesian Age model for VIL sequence with all the dates included (A) and the final result with the 30 selected dates and the main sedimentation rate changes indicated (B).

A)

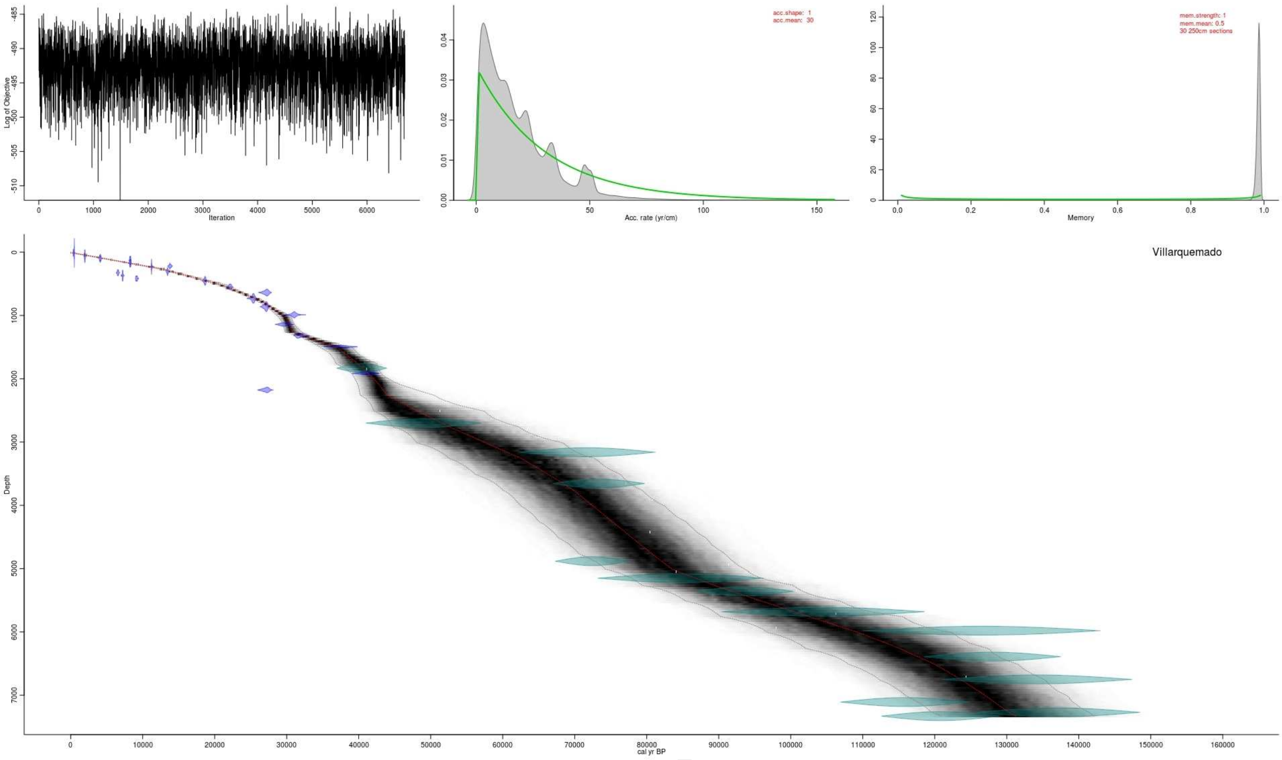

B)

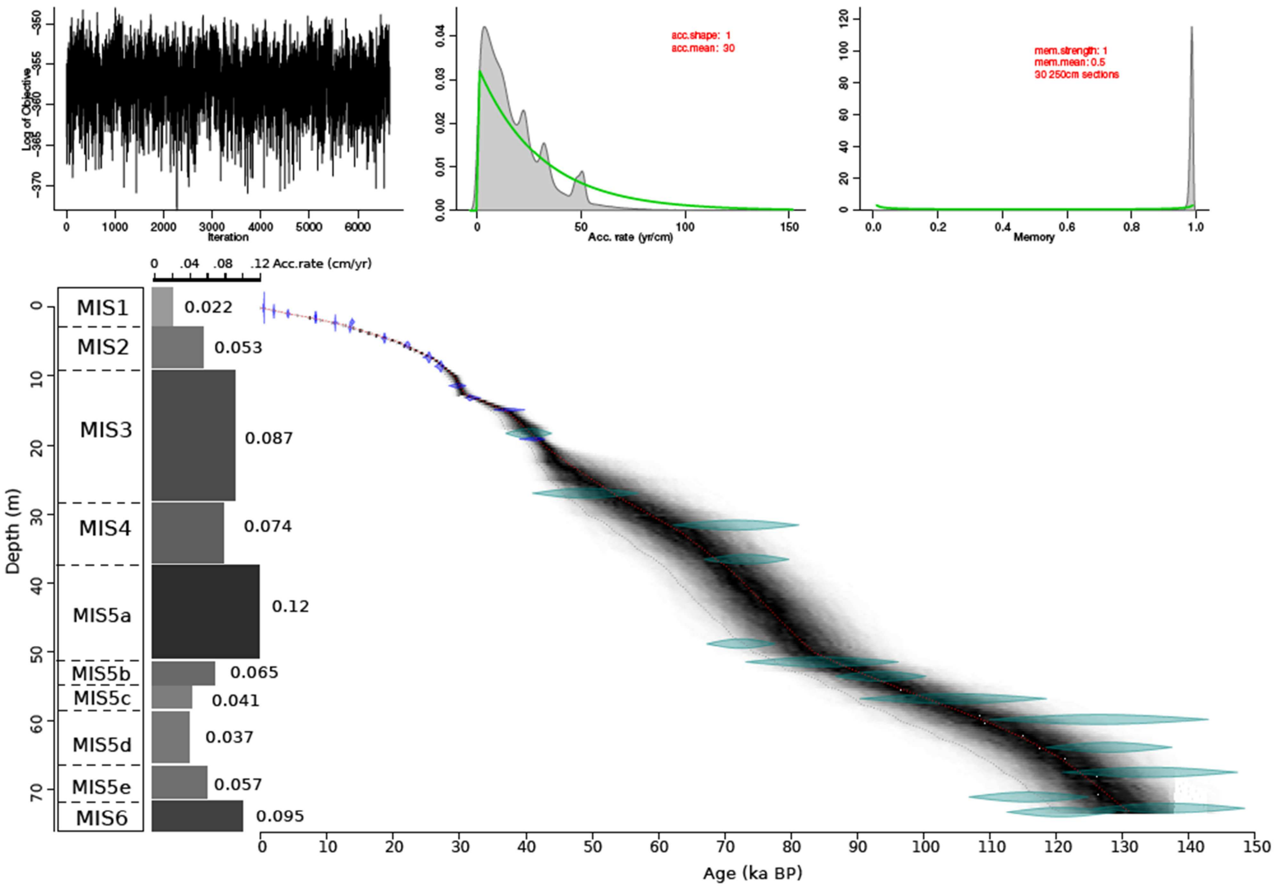
Log of Objective
Iteration
Acc. rate (yr/cm)
acc.shape: 1
acc.mean: 30
Memory
mem.strength: 1
mem.mean: 0.5
30 250cm sections
0 .04 .08 .12 Acc.rate (cm/yr)
MIS1
0.022
MIS2
0.053
MIS3
0.087
MIS4
0.074
MIS5a
0.12
MIS5b
0.065
MIS5c
0.041
MIS5d
0.037
MIS5e
0.057
MIS6
0.095
Depth (m)
Age (ka BP)

Figure 6. Main geochemical and palynological data of VIL sequence plotted in age with both sedimentological units (on the left) and MIS periods (on the right) indicated. Chronological limits for MIS periods follow Lisiecki and Raymo (2005) and Rasmussen et al. (2014) while stadials and interstadials into MIS 5 chronology follow Martrat et al. (2004). Pollen groups are composed by the following taxa: Mediterranean includes evergreen *Quercus, Viburnum, Buxus,* Oleaceae, *Pistacia, Rhamnus, Myrtus,* Thymelaeaceae*, Arbutus unedo*, Cistaceae and *Helianthemum*. Steppe includes *Ephedra distachya* and *E. fragilis* types and Chenopodiaceae. Local moisture is formed by aquatics and Pterydophyta: Cyperaceae, Typhaceae, *Juncus, Sparganium, Thalictrum, Lythrum, Stratiotes, Utricularia*, *Ledum palustre, Ranunculus, Pedicularis, Myriophyllum, Lemna, Nymphaea, Nuphar, Potamogeton, Isoetes, Alisma, Callitriche, Asplenium*, Monolete, Trilete, *Polypodium, Botrychium, Pteris, Equisetum* and *Selaginella.* Shaded grey bands show intervals with low pollen productivity in MIS 5b, MIS 3 and MIS 2.

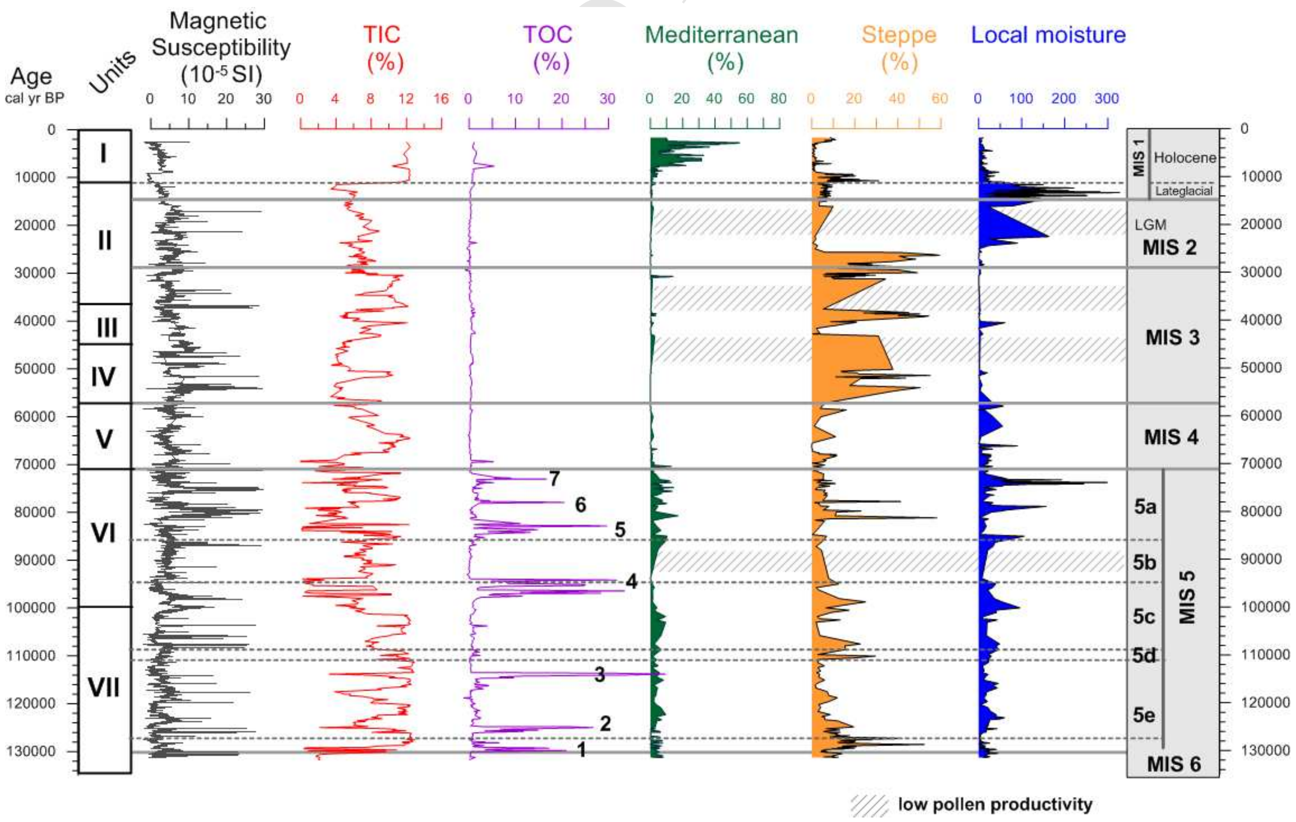

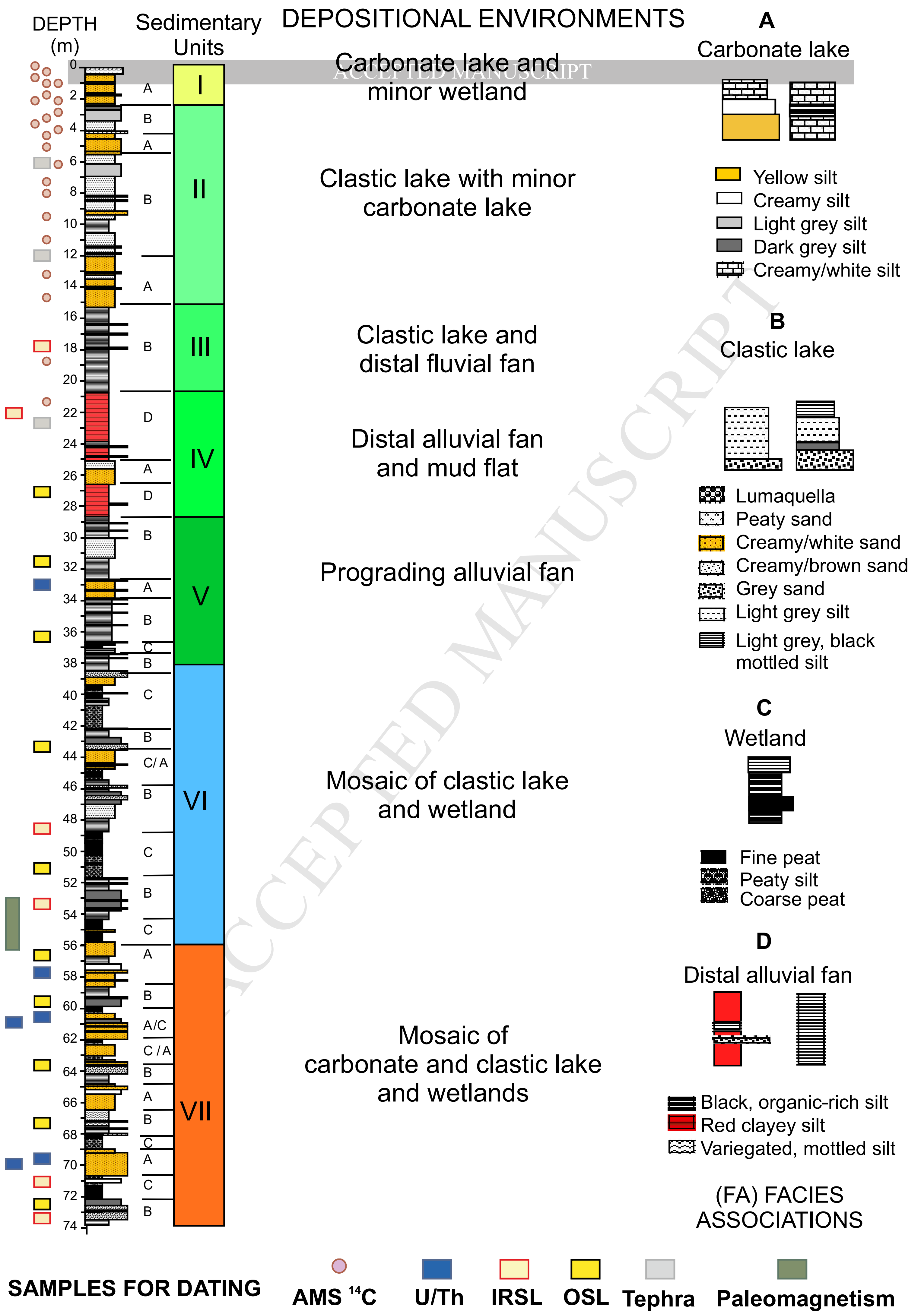

DEPTH (m)
Sedimentary Units
DEPOSITIONAL ENVIRONMENTS
Carbonate lake and minor wetland
Clastic lake with minor carbonate lake
Clastic lake and distal fluvial fan
Distal alluvial fan and mud flat
Prograding alluvial fan
Mosaic of clastic lake and wetland
Mosaic of carbonate and clastic lake and wetlands
I
II
III
IV
V
VI
VII
A
Carbonate lake
Yellow silt
Creamy silt
Light grey silt
Dark grey silt
Creamy/white silt
B
Clastic lake
Lumaquella
Peaty sand
Creamy/white sand
Creamy/brown sand
Grey sand
Light grey silt
Light grey, black mottled silt
C
Wetland
Fine peat
Peaty silt
Coarse peat
D
Distal alluvial fan
Black, organic-rich silt
Red clayey silt
Variegated, mottled silt
(FA) FACIES ASSOCIATIONS
SAMPLES FOR DATING
AMS ^{14}C
U/Th
IRSL
OSL
Tephra
Paleomagnetism